

UNIVERSITY OF OKLAHOMA  
GRADUATE COLLEGE

This is the thesis title

A DISSERTATION  
SUBMITTED TO THE GRADUATE FACULTY  
in partial fulfillment of the requirements for the  
Degree of  
DOCTOR OF PHILOSOPHY

By  
YU-TING SHEN  
Norman, Oklahoma  
2017

This is the thesis title

A DISSERTATION APPROVED FOR THE  
HOMER L. DODGE DEPARTMENT OF PHYSICS AND ASTRONOMY

BY

---

Dr. Patrick Skubic, Chair

---

Dr. Michael Strauss

---

Dr. Ron Kantowski

---

Dr. Deborah Watson

---

Dr. S. Lakshmivaran



*‘Blood, sweat & respect. First two you give, last one you earn.’*

- Dwayne Johnson

# Acknowledgements

I would like to thank everyone who have helped me. Especially thanks to my advisor Patrick Skubic, SS/3L + jets analysis convenor Ximo Poveda Torres, and post doctor Judita Mamužić.

# Contents

	Page
<b>List of Tables</b>	<b>vii</b>
<b>List of Figures</b>	<b>ix</b>
<b>1 Introduction</b>	<b>1</b>
<b>2 The Standard Model</b>	<b>5</b>
2.1 The Standard Model of Particle Physics . . . . .	5
2.1.1 Particle Content . . . . .	6
2.1.2 Local Gauge Theory . . . . .	9
2.1.3 Strong interaction . . . . .	10
2.1.4 Electroweak interaction . . . . .	11
2.1.5 The discovery of Higgs boson . . . . .	16
2.2 Beyond the Standard Model . . . . .	17
2.2.1 Hierarchy problem . . . . .	18
2.2.2 Dark matter and dark energy . . . . .	18
2.2.3 Grand Unification . . . . .	19
2.2.4 More questions . . . . .	19
<b>3 Supersymmetry</b>	<b>21</b>
3.1 Why supersymmetry . . . . .	21
3.2 Introduction of the supersymmetry . . . . .	24
3.2.1 Superalgebra . . . . .	24
3.2.2 Superspace and superfields . . . . .	26
3.2.3 $R$ -parity . . . . .	28
3.2.4 Supersymmetry breaking . . . . .	28
3.2.5 The Minimal Supersymmetry Standard Model . . . . .	29
3.3 The radiative natural SUSY . . . . .	30
3.4 The non-universal Higgs model with two extra parameters . . . . .	32
<b>4 The ATLAS Experiment at LHC</b>	<b>34</b>
4.1 The Large Hadron Collider . . . . .	35
4.2 The ATLAS experiment . . . . .	38
4.2.1 The ATLAS coordinate system . . . . .	39
4.2.2 The inner detector and tracking system . . . . .	40
4.2.3 The calorimeters . . . . .	43
4.2.4 The muon spectrometer . . . . .	48
4.2.5 The trigger system and data acquisition . . . . .	50

<b>5</b>	<b>Data set and simulated events</b>	<b>53</b>
5.1	Collision data . . . . .	53
5.2	Monte Carlo simulated event samples . . . . .	54
5.2.1	The SM background samples . . . . .	55
5.2.2	The SUSY signal samples . . . . .	55
<b>6</b>	<b>Event reconstruction and selection</b>	<b>62</b>
<b>7</b>	<b>Background estimation</b>	<b>63</b>
<b>8</b>	<b>Results</b>	<b>64</b>
<b>9</b>	<b>Conclusion</b>	<b>65</b>
	<b>Appendix</b>	<b>67</b>
<b>A</b>	<b>Simulated samples</b>	<b>67</b>
A.1	Samples used for strong interaction . . . . .	67
A.2	Samples used for weak interaction . . . . .	67
<b>B</b>	<b>Cross-sections of NUHM2</b>	<b>69</b>
<b>C</b>	<b>Electron reconstruction, identification, and isolation</b>	<b>78</b>
C.1	Electron reconstruction . . . . .	78
C.2	Electron identification . . . . .	79
C.3	Electron isolation . . . . .	79
<b>D</b>	<b>Real lepton efficiency</b>	<b>80</b>
	<b>References</b>	<b>81</b>

# List of Tables

	Page
2.1 The Standard Model fermions with charges and masses [29]. . . . .	7
2.2 The four fundamental forces with the relative strength, interaction range, describing theory, and the mediator with its mass. The gravitational force is not a part of the SM and the graviton is a theoretical particle. . . . .	8
3.1 Chiral supermultiplets and gauge supermultiplets in the MSSM. In the chiral supermultiplets, the spin 0 fields are complex scalars and the spin 1/2 fields are left-handed two-component Weyl spinors. . . . .	30
4.1 Resolution requirements for the different calorimeters of the ATLAS detector [66].	47
4.2 A summary of the muon spectrometer components. . . . .	50
5.1 The inclusive $E_T^{\text{miss}}$ triggers used in this analysis. The $E_T^{\text{miss}}$ threshold varies from 70 to 110 GeV depending on the run period. . . . .	54
5.2 The MC simulated samples of SM background process. . . . .	56
5.3 The masses of $\tilde{\chi}_1^0$ , $\tilde{\chi}_2^0$ , and $\tilde{\chi}_1^\pm$ and the ratios of the mass difference between $(m_{\tilde{\chi}_2^0} - m_{\tilde{\chi}_1^\pm})$ and $(m_{\tilde{\chi}_1^\pm} - m_{\tilde{\chi}_1^0})$ . . . . .	57
5.4 The possible $\tilde{\chi}_2^0$ decays in NUHM2 with $m_{1/2} = 600$ GeV. The $\tilde{\chi}_2^0 \rightarrow \gamma\tilde{\chi}_1^0$ has the lowest branching ratio hence it is not considered in our study. The rest of the decays are categorized into 4 types as shown in the third column. . . . .	60
5.5 The 2 leptons filter efficiency for 4 kinds of $\tilde{\chi}_2^0$ decay, the number of events for each decay in $0 < m_{\ell\ell} < 50$ GeV, and the contributions to the whole $\tilde{\chi}_2^0$ decay. The transverse momentum of 2 leptons are required to be greater than 2 GeV and no $E_T^{\text{miss}}$ requirement is applied in the filter. . . . .	61
A.1 The simulated signal and background MC samples. The event generator, parton shower, cross-section normalization, PDF set, and the set of tuned parameters for each samples are shown. The $t\bar{t}WW$ , $t\bar{t}WZ$ , $tZ$ , $tWZ$ , $t\bar{t}\bar{t}$ , $WH$ , $ZH$ and triboson background samples are labeled in the "rare" because they contribute a very small amount to the signal region. . . . .	68
B.1 The cross-sections, branching fraction, and filter efficiency for the NUHM2 signal samples $m_{1/2} = 300$ GeV. . . . .	70
B.2 The cross-sections, branching fraction, and filter efficiency for the NUHM2 signal samples $m_{1/2} = 350$ GeV. . . . .	71
B.3 The cross-sections, branching fraction, and filter efficiency for the NUHM2 signal samples $m_{1/2} = 400$ GeV. . . . .	72
B.4 The cross-sections, branching fraction, and filter efficiency for the NUHM2 signal samples $m_{1/2} = 500$ GeV. . . . .	73
B.5 The cross-sections, branching fraction, and filter efficiency for the NUHM2 signal samples $m_{1/2} = 600$ GeV. . . . .	74



B.6	The cross-sections, branching fraction, and filter efficiency for the NUHM2 signal samples $m_{1/2} = 700$ GeV. . . . .	75
B.7	The cross-sections, branching fraction, and filter efficiency for the NUHM2 signal samples $m_{1/2} = 800$ GeV. . . . .	76
B.8	The list of various final states. . . . .	77

# List of Figures

	Page
1.1 The scatter plot in the $m(\tilde{\chi}_1^0)$ vs $m(\tilde{\chi}_1^\pm)$ plane. The color encode the $\tilde{\chi}_1^0$ composition. The Higgsino-dominated LSPs are colored in yellow and along the $\tilde{\chi}_1^0$ - $\tilde{\chi}_1^\pm$ diagonal. The figure is taken from [13]. . . . .	2
1.2 The Feynman diagrams representing the two leptons final statw of (a) $\tilde{\chi}_2^0\tilde{\chi}_1^\pm$ , (b) $\tilde{\chi}_1^\pm\tilde{\chi}_1^\mp$ , (c) $\tilde{\chi}_2^0\tilde{\chi}_1^0$ productions. . . . .	3
2.1 An illustration of the Higgs potential which has the form of a Mexican hat. The figure is taken from [40]. . . . .	15
2.2 The observed local $p$ -value as a function of $m_H$ for the ATLAS [1] and CMS [2] experiment, respectively. The dashed line shows the expected local $p_0$ for a SM Higgs boson. The horizontal lines denotes the $p$ -values corresponding to significances of 1 to $6\sigma$ . . . . .	17
2.3 The measured running coupling constants in the SM (left) and prediction in the GUT (right). The three lines show the inverse value of the coupling constant for the three fundamental forces. This figure is taken from [48]. . . . .	20
3.1 The Feymann diagram for the one loop correction to the Higgs squared mass due to (a) a fermion $f$ and (b) a scalar $S$ . The figure is taken from [9]. . . . .	22
4.1 The accelerator complex at CERN [73]. . . . .	36
4.2 Overview of the ATLAS detector [66]. . . . .	38
4.3 Cut-away view of the ATLAS inner detector [66]. . . . .	41
4.4 Cut-away view of the calorimeter system [66]. . . . .	44
4.5 Cut-away view of the accordion shaped EMB module with the dimensions for three layers [76]. . . . .	46
4.6 Sketch of the muon system of the ATLAS detector [66]. . . . .	49
4.7 The schematic view of the ATLAS trigger/DAQ system in Run-2. The figure is taken from [80]. . . . .	51
5.1 The mass spectra of the charginos $\tilde{\chi}_{1,2}^\pm$ and neutralinos $\tilde{\chi}_{1,2,3,4}^0$ as a function of $m_{1/2}$ in the NUHM2 model. The $m_{\tilde{\chi}_1^0}$ , $m_{\tilde{\chi}_2^0}$ , and $m_{\tilde{\chi}_1^\pm}$ are roughly flat when $m_{1/2} > 500$ GeV. The $m_{\tilde{\chi}_3^0}$ , $m_{\tilde{\chi}_4^0}$ , and $m_{\tilde{\chi}_2^\pm}$ are heavier and increase with $m_{1/2}$ . .	57
5.2 The mass splitting spectra between charginos and neutralinos in the NUHM2 model. The mass differences between $(\tilde{\chi}_3^0, \tilde{\chi}_{1,2}^0)$ and $(\tilde{\chi}_3^0, \tilde{\chi}_1^\pm)$ increase with $m_{1/2}$ . The mass differences between $(\tilde{\chi}_1^\pm, \tilde{\chi}_1^0)$ , $(\tilde{\chi}_2^0, \tilde{\chi}_1^0)$ , and $(\tilde{\chi}_2^0, \tilde{\chi}_1^\pm)$ decress with $m_{1/2}$ . .	57
5.3 The NUHM2 cross-sections. The cross-sections of individual combination are presented in dashed lines and the cross-sections for compressed + compressed, compressed + accessible, and accessible + accessible are represented in solid lines. .	58

# Chapter 1

## Introduction

The Standard Model of particle physics (SM) describes various phenomena of particle physics. The discovery of the Higgs boson ( $H$ ) by the ATLAS and CMS collaboration at CERN completes the missing part of the SM prediction [1, 2]. However, there are several open challenges that cannot be explained by the SM, such as hierarchy problem [3, 4, 5] and the dark matter candidate. In order to answer those questions, a new theory extending the SM is necessary. Supersymmetry (SUSY) [6, 7, 8, 9] is the most promising extensions of the SM. SUSY, which is a spacetime symmetry, introduces the superpartners of SM particles (sparticles) with spin differing by one-half unit with respect to the SM partners. The sparticles provide a potential solution to the hierarchy problem. If  $R$ -parity is conserved [10, 11, 12], the sparticles are produced in pairs and the lightest SUSY particle (LSP) is stable providing the candidate for dark matter.

The charginos  $\tilde{\chi}_{1,2}^{\pm}$  and neutralinos  $\tilde{\chi}_{1,2,3,4}^0$  are the mass eigenstates in the order of increasing masses and collectively referred to as electroweakinos. They are the mixture of the bino  $\tilde{B}$ , winos  $\tilde{W}$ , and higgsinos  $\tilde{H}_{u,d}$  which are the superpartners of the  $U(1)$ ,  $SU(2)$  gauge bosons, and the Higgs bosons, respectively. The charginos and neutralinos can decay into leptons and LSPs via  $W$ ,  $Z$ ,  $H$  or sleptons  $\tilde{\ell}$ . In many SUSY models, the lightest neutralino  $\tilde{\chi}_1^0$  is the LSP. The LSP couldn't be detected and results in significant

missing transverse energy  $E_T^{\text{miss}}$ .

The compressed scenarios refer to the small mass differences between heavier SUSY particles and the LSP. For example, the mass differences between the heavier electroweakino states  $\tilde{\chi}_2^0$ ,  $\tilde{\chi}_1^\pm$  and the wino- or higgsino-dominated LSP  $\tilde{\chi}_1^0$  range from a few MeV to tens of GeV depending on the composition of the mixture. The  $\tilde{B}$ ,  $\tilde{W}$ , and  $\tilde{H}$  composition of the  $\tilde{\chi}_1^0$  have an influence on the degree of compression. Figure 1.1 shows the composition of the lightest neutralino in a MSSM scan of the electroweakino sector [13]. Based on naturalness arguments [14, 15], the Higgsino mass parameter  $\mu$ , the bino and wino mass parameters  $M_1$  and  $M_2$  satisfy  $|\mu| \ll |M_1|, |M_2|$  leading to the three electroweakinos  $\tilde{\chi}_1^0$ ,  $\tilde{\chi}_1^\pm$ , and  $\tilde{\chi}_2^0$  being dominated by the Higgsino.

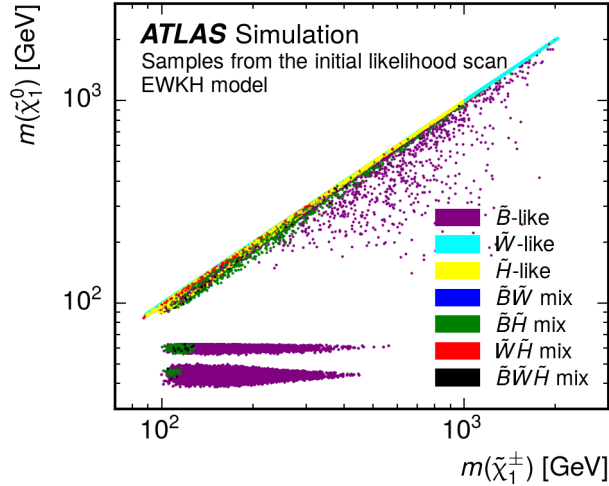


**Figure 1.1:** The scatter plot in the  $m(\tilde{\chi}_1^0)$  vs  $m(\tilde{\chi}_1^\pm)$  plane. The color encode the  $\tilde{\chi}_1^0$  composition. The Higgsino-dominated LSPs are colored in yellow and along the  $\tilde{\chi}_1^0$ - $\tilde{\chi}_1^\pm$  diagonal. The figure is taken from [13].

This dissertation focuses on searching for electroweak production SUSY particles in compressed scenarios with exactly two low-momentum same-flavor opposite-charged leptons in final states and missing transverse momentum  $\mathbf{p}_T^{\text{miss}}$ . This search uses proton-

proton collision data at  $\sqrt{s} = 13$  TeV recorded by the ATLAS detector at the Large Hadron Collider (LHC) [16] in 2015 and 2016, corresponding to a total integrated luminosity of  $36.1 \text{ fb}^{-1}$ . Figure 1.2 shows the Feynman diagrams representing the electroweakino productions with two leptons final state in association with an initial state radiated jet. Same-flavor opposit-charged leptons come from the  $\tilde{\chi}_2^0$  decays in the  $\tilde{\chi}_2^0\tilde{\chi}_1^\pm$  and  $\tilde{\chi}_2^0\tilde{\chi}_1^0$  productions, and from the  $\tilde{\chi}_1^\pm$  decays in  $\tilde{\chi}_1^\pm\tilde{\chi}_1^\mp$  production. The two leptons can be reconstructed in the detector and carry small transverse momentum  $p_T$  hence they are very soft. However, the two LSPs are invisible and back-to-back in the rest fram of their parent electroweakinos. Because they carry large momentum, the missing transverse energy  $E_T^{\text{miss}}$  is relatively large.

Similar searches have been performed using  $\sqrt{s} = 8$  TeV and  $\sqrt{s} = 13$  TeV by the ATLAS [17, 18, 19, 13] and CMS [20, 21, 22] experiments. Combining with the results from the LEP experiments, the mass limits for sleptons and charginos are  $m(\tilde{e}_R) > 73$  GeV,  $m(\tilde{\mu}_R) > 94.6$  GeV, and  $m(\tilde{\chi}_1^\pm) > 103.5$  GeV or 92.4 GeV depending on the  $\Delta m(\tilde{\chi}_1^0, \tilde{\chi}_1^\pm)$ .

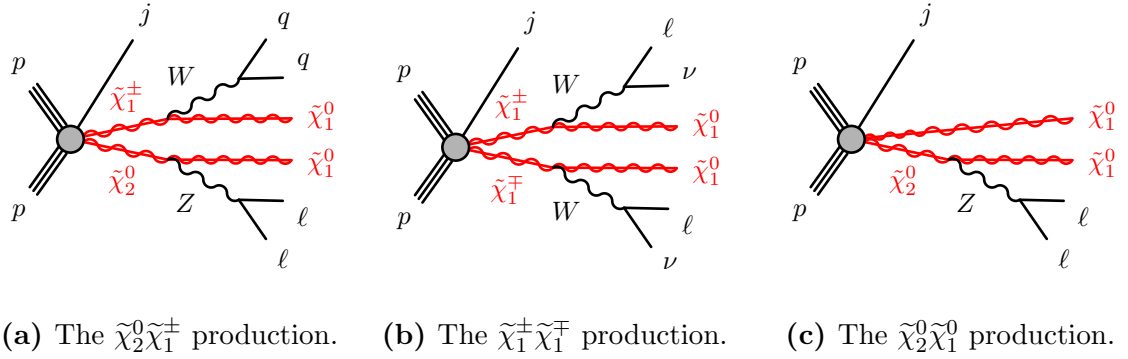


**Figure 1.2:** The Feynman diagrams representing the two leptons final statw of (a)  $\tilde{\chi}_2^0\tilde{\chi}_1^\pm$ , (b)  $\tilde{\chi}_1^\pm\tilde{\chi}_1^\mp$ , (c)  $\tilde{\chi}_2^0\tilde{\chi}_1^0$  productions.

This dissertation has the following structure. After introducing the theoretical fundations in the Chapters 2 and 3, the experiment facilities are described in Chapter 4.

The data and Monte Carlo samples used in this analysis are detailed in Chapter 5. The event reconstruction and selection are outlined in Chapter 6. The background estimation and the systematic uncertainties are addressed in Chapter 7. Finally, the results and the conclusions are presented in Chapter 8 and Chapter 9.

# Chapter 2

## The Standard Model

This chapter outlines the theoretical and mathematical concepts of the high energy particle physics. The Standard Model of particle physics (SM) [23, 24, 25, 26, 27] is developed since the early 1970s and it has successfully explained almost all experimental results. The SM is a well-tested and the most successful physics theory to describe the nature of the elementary particles and their interactions. An overview of the SM is given in Section 2.1. After that, some of the open questions are mentioned in Section 2.2.

### 2.1 The Standard Model of Particle Physics

The Standard Model of particle physics is known as the most accurate theory for describing the elementary particles and the interactions between them. By combining the quantum mechanics and special relativity, the SM is a relativistic *Quantum Field Theory* (QFT) based on a  $SU(3)_C \otimes SU(2)_L \otimes U(1)_Y$  symmetry gauge group, where  $C$  denotes colour,  $L$  represents left chirality, and  $Y$  stands for weak hypercharge, respectively. The  $SU(3)_C$  group is the basis for *Quantum Chromodynamics* (QCD) which describes the strong interaction and the  $SU(2)_L \otimes U(1)_Y$  group is the foundation of the electroweak interaction which unifies the electromagnetic and weak interactions. Therefore, the SM Lagrangian

is invariant under the local gauge transformation. According to *Noether's Theorem* [28], the invariance of an action of a physical system undergoes a symmetry transformation corresponding to a conservation law and vice versa. The gauge invariance of the SM Lagrangian corresponds to the conserved quantum numbers, or the charges, of each interaction. The conserved charges are the three colour charge (red, blue, green) for the strong interaction, the third component of the weak isospin  $I_3$  for the weak interaction, and the electric charge  $Q$  for the electromagnetic interaction.

### 2.1.1 Particle Content

According to the SM, all matter around us is made of elementary particles called *quarks* and *leptons*. The quarks and leptons are called fermions which have half integral spin  $s = \frac{1}{2}$ , hence the fermions follow the Pauli exclusion principle which says no two fermions have the same quantum state at the same time. Each fermion has an anti-fermion with the equal mass but carries opposite electric charge, weak isospin and colour charge. There are six quarks and six leptons, they are grouped into three pairs, or "*generations*", ordered by their mass. The lightest and most stable particles constitute the first generation and they are constituents of ordinary matter. The heavier and less stable particles form the second and third generations and the heavier particles quickly decay to the next most stable particles. The three generations of quarks are up ( $u$ ) and down ( $d$ ), charm ( $c$ ) and strange ( $s$ ), and top ( $t$ ) and bottom ( $b$ ) quarks. The up-type quarks ( $u, c, t$ ) carry  $+\frac{2}{3}|e|$  charge and with isospin  $+\frac{1}{2}$  while the down-type quarks ( $d, s, b$ ) carry  $-\frac{1}{3}|e|$  charge with isospin  $-\frac{1}{2}$ . The quarks carry an additional colour charge of either red, green, or blue, and hence they only interact via the strong force. Because the strong force holds quarks together, only non-integer charges of the quark combinations are experimentally allowed. The quark



combinations are called *hadrons* which can be categorised into *mesons* and *baryons*. The meson is composed by a quark and anti-quark pair ( $q\bar{q}$ ) whereas the baryon is made up by three quarks ( $qqq$  or  $\bar{q}\bar{q}\bar{q}$ ). Only colourless bound states of hadrons are allowed so the quark and anti-quark pair in a meson should contain colour and anti-colour and the three quarks in a baryon must carry different colours. The leptons are colourless and are therefore participating in the weak and electromagnetic force only. They do not participate in the strong interaction. The electron-type leptons ( $e, \mu, \tau$ ) carry an elementary charge  $|e|$  and their corresponding neutrinos ( $\nu_e, \nu_\mu, \nu_\tau$ ) are neutral. The neutrinos have very little mass and interact via weak force only. A summarised table of the properties of quarks and leptons is given in Table 2.1.

Generation	Fermion	particle	electric charge $Q$	weak isospin $I_3$	colour charge $C$	mass [GeV]	
I	Quark	$u$	up quark	$+\frac{2}{3} e $	$+\frac{1}{2}$	r,g,b	0.0023
		$d$	down quark	$-\frac{1}{3} e $	$-\frac{1}{2}$	r,g,b	0.0048
	Lepton	$e$	electron	$-1 e $	$-\frac{1}{2}$	-	0.00051
		$\nu_e$	electron neutrino	0	$+\frac{1}{2}$	-	$< 2 \times 10^{-9}$
II	Quark	$c$	charm quark	$+\frac{2}{3} e $	$+\frac{1}{2}$	r,g,b	1.275
		$s$	strange quark	$-\frac{1}{3} e $	$-\frac{1}{2}$	r,g,b	0.095
	Lepton	$\mu$	muon	$-1 e $	$-\frac{1}{2}$	-	0.106
		$\nu_\mu$	muon neutrino	0	$+\frac{1}{2}$	-	$< 1.9 \times 10^{-7}$
III	Quark	$t$	top quark	$+\frac{2}{3} e $	$+\frac{1}{2}$	r,g,b	173.2
		$b$	bottom quark	$-\frac{1}{3} e $	$-\frac{1}{2}$	r,g,b	4.18
	Lepton	$\tau$	tau	$-1 e $	$-\frac{1}{2}$	-	1.777
		$\nu_\tau$	tau neutrino	0	$+\frac{1}{2}$	-	$< 1.82 \times 10^{-5}$

**Table 2.1:** The Standard Model fermions with charges and masses [29].

There are four fundamental forces in the universe: the strong force, the weak force, the electromagnetic force, and the gravitational force. The first three forces are described in the SM, however, the gravitational force could not yet be included in the SM. Because

the effect of the gravitational force is very weak and can be negligible, the SM works well without considering the gravitational force. Each force has a force-carrier particle called gauge boson and there is a quantum number associate to it. The gauge bosons of the strong force are eight massless *gluons*,  $g$ , which associate to colour charge  $C$ . The gauge bosons of the weak force are  $W^\pm$  and  $Z^0$  bosons which associate to weak isospin  $I_3$ . The gauge boson of the electromagnetic force is massless *photon*,  $\gamma$ , which associates to electric charge  $Q$ . Although the gluon and photon are massless particles, the  $W^\pm$  and  $Z^0$  bosons are massive. The mass of the  $W^\pm$  and  $Z^0$  bosons are  $m_W = 80.385 \pm 0.015$  GeV and  $m_Z = 91.1876 \pm 0.0021$  GeV [29], respectively. Table 2.2 shows the four fundamental forces, the relative strength and range together with the theories and the mediators.

Force	Rel. Strength	Range [m]	Theory	Mediator	Mass [GeV]
Strong	10	$10^{-15}$	Chromodynamics	Gluon	0
Weak	$10^{-13}$	$10^{-18}$	Flavourdynamics	$W^\pm$ and $Z^0$ bosons	80.4/91.2
Electromagnetic	$10^{-2}$	$\infty$	Electrodynamics	Photon	0
Gravitational	$10^{-42}$	$\infty$	General relativity	Graviton	-

**Table 2.2:** The four fundamental forces with the relative strength, interaction range, describing theory, and the mediator with its mass. The gravitational force is not a part of the SM and the graviton is a theoretical particle.

### 2.1.2 Local Gauge Theory

The Lagrangian density of the SM for the free fields<sup>1</sup> listed in the Equation 2.1 is invariant under local gauge transformation<sup>2</sup>

$$\mathcal{L} = \bar{\psi}(i\gamma^\mu\partial_\mu - m)\psi + e\bar{\psi}\gamma^\mu\psi\mathbf{A}_\mu - \frac{1}{4}\mathbf{F}_{\mu\nu}\mathbf{F}^{\mu\nu} \quad (2.1)$$

where  $\mathbf{F}_{\mu\nu} = \partial_\mu\mathbf{A}_\nu - \partial_\nu\mathbf{A}_\mu$ . The local gauge transformation means the scalar field  $\psi$  and the vector field  $\mathbf{A}_\mu$  transform as

$$\psi(x) \rightarrow \psi'(x) = e^{i\theta(x)}\psi(x) \quad (2.2)$$

$$\mathbf{A}_\mu(x) \rightarrow \mathbf{A}'_\mu(x) = \mathbf{A}_\mu(x) + \frac{1}{e}\partial_\mu\theta(x). \quad (2.3)$$

By introducing the gauge term, i.e. the vector field, the interacting force can be obtained by calculating the derivatives of the *Euler-Lagrange equations*. The gauge field can be associated to particular spin one gauge bosons which mediate the force. The number of the mediating gauge bosons is equal to the dimension of the symmetry group. From the group theory, the dimension of an unitary group  $U(n)$  is  $n^2$  and the dimension of a special unitary group  $SU(n)$  is  $n^2 - 1$ . Because the SM is based on a  $SU(3)_C \otimes SU(2)_L \otimes U(1)_Y$  symmetry gauge group, the number of mediators are 8 for  $SU(3)_C$ , 3 for  $SU(2)_L$ , and 1 for  $U(1)_Y$  corresponding to 8 gluons for the strong interaction, 3 gauge bosons ( $W^\pm$  and  $Z^0$ ) for weak interaction, and 1 photon for the electromagnetic interaction.

---

<sup>1</sup>This is the Lagrangian density of QED. The three terms are fermion kinematic term, photon kinematic term, and interaction, respectively.

<sup>2</sup>In Dirac representation, the four contravariant gamma matrices are  $\gamma^0 = \begin{pmatrix} 1 & 0 & 0 & 0 \\ 0 & 1 & 0 & 0 \\ 0 & 0 & -1 & 0 \\ 0 & 0 & 0 & -1 \end{pmatrix}$ ,  $\gamma^1 = \begin{pmatrix} 0 & 0 & 0 & 1 \\ 0 & 0 & 1 & 0 \\ 0 & -1 & 0 & 0 \\ -1 & 0 & 0 & 0 \end{pmatrix}$ ,  $\gamma^2 = \begin{pmatrix} 0 & 0 & 0 & -i \\ 0 & 0 & i & 0 \\ 0 & i & 0 & 0 \\ -i & 0 & 0 & 0 \end{pmatrix}$ ,  $\gamma^3 = \begin{pmatrix} 0 & 0 & 1 & 0 \\ 0 & 0 & 0 & -1 \\ -1 & 0 & 0 & 0 \\ 0 & 1 & 0 & 0 \end{pmatrix}$

### 2.1.3 Strong interaction

The *Quantum Chromodynamics* (QCD) is the theory to describe the strong interaction. The gauge bosons are the eight massless gluons which carry three different colours (and anti-colours), red, green, and blue. Quarks interact with gluons hence they also carry colour charge  $C$  and can be represented in colour triplets

$$\psi = \begin{pmatrix} \psi_r \\ \psi_g \\ \psi_b \end{pmatrix}. \quad (2.4)$$

The QCD is based on the non-Abelian  $SU(3)_C$  group which requires local gauge transformation

$$\psi \rightarrow \psi' = e^{ig_s \alpha_a(x) T^a} \psi \quad (2.5)$$

where the  $g_s$  is the strong coupling constant,  $\alpha_a(x)$  are arbitrary functions of space-time, and  $T^a$  are the generators of the non-Abelian  $SU(3)_C$  group and the summation over  $a$  with  $a = 1, \dots, 8$  is implied. The Lagrangian density is invariant under the local gauge transformation by introducing the new form of the gauge fields and the covariant derivative

$$\mathbf{G}_\mu^a \rightarrow \mathbf{G}_\mu^a - \partial_\mu \alpha^a(x) - g_s f_{abc} \alpha^b(x) \mathbf{G}_\mu^c \quad (2.6)$$

$$\partial_\mu \rightarrow D_\mu = \partial_\mu + ig_s T_a \mathbf{G}_\mu^a \quad (2.7)$$

where  $f_{abc}$  is the structure constant. The Lagrangian density of QCD is given by

$$\mathcal{L}_{QCD} = \bar{\psi}(i\gamma^\mu \partial_\mu - m)\psi - g_s(\bar{\psi}\gamma^\mu T_a \psi)\mathbf{G}_\mu^a - \frac{1}{4}\mathbf{G}_{\mu\nu}^a \mathbf{G}_a^{\mu\nu} \quad (2.8)$$

where the field strength tensor  $\mathbf{G}_{\mu\nu}^a = \partial_\mu \mathbf{G}_\nu^a - \partial_\nu \mathbf{G}_\mu^a - g_s f_{abc} \mathbf{G}_\mu^b \mathbf{G}_\nu^c$  causing self-interactions between the gluons. The strong force increases with distance between quarks, therefore, the quarks exist only as colourless compounds such as meson or baryon mentioned in

Section 2.1.1. The production of a single quark is accompanied by the creation of an anti-quark from vacuum to form a quark and anti-quark pair as a colourless compound. This is called *hadronisation*. The phenomena that confined quarks in the small interaction range is called *confinement*. But at small distance or high energy, the quarks can be considered as quasi-free particles. This is referred to as *asymptotic freedom*.

#### 2.1.4 Electroweak interaction

Fermi formulated the first weak interaction theory in 1933 [30], however, the theory only holds for energies less than 100 GeV. Glashow, Salam, and Weinberg (GSW) proposed a new model [23, 25, 24] which unifies electromagnetic and weak forces to become *electroweak* (EW) force and this new *GSW model* can apply to the energy greater than 100 GeV. The electroweak theory is based on  $SU(2)_L \otimes U(1)_Y$  gauge symmetry where the subscripts  $L$  denotes the left-handedness because only the left-handed fermions (and right-handed anti-fermions) and  $Y$  denotes the weak hypercharge, a new quantum number, which relates to the electric charge  $Q$  and the weak isospin  $I_3$  by the *Gell-Mann-Nishijima relation* [31, 32]

$$Y = 2(Q - I_3). \quad (2.9)$$

The left-handed and right-handed fermion field  $\psi$  can be decomposed into two components

$$\psi = P_L \psi + P_R \psi \quad (2.10)$$

$$= \psi_L + \psi_R \quad (2.11)$$

where the projection operators  $P_L$  and  $P_R$  are defined as<sup>3</sup>

$$P_L = \frac{1}{2}(1 - \gamma^5) \quad (2.12)$$

$$P_R = \frac{1}{2}(1 + \gamma^5). \quad (2.13)$$

The projection operators satisfy  $P_L P_R = 0$  and  $P_L + P_R = 1$ . Experimental observations show the right-handed neutrinos don't participate in all the interactions described in the SM so the  $\psi_R$  is a singlet and  $I_3 = 0$ <sup>4</sup>. The local gauge transformations of the  $SU(2)_L \otimes U(1)_Y$  are

$$\psi_L \rightarrow \psi'_L = e^{i\alpha_a(x)T^a} e^{i\beta(x)Y} \psi_L \quad (2.14)$$

$$\psi_R \rightarrow \psi'_R = e^{i\beta(x)Y} \psi_R \quad (2.15)$$

where  $T^a = \frac{\sigma^a}{2}$  are the generators of  $SU(2)_L$  with Pauli matrix  $\sigma^a$ <sup>5</sup> and  $Y$  is the generator of  $U(1)_Y$ . The  $\alpha_a(x)$  and  $\beta(x)$  depend on the space-time. The covariant derivative with respect to the  $SU(2)_L \otimes U(1)_Y$  is

$$D_\mu = \partial_\mu + ig_W T_a \mathbf{W}_\mu^a + ig_Y Y \mathbf{B}_\mu \quad (2.16)$$

where  $g_W$  and  $g_Y$  are coupling constants and  $\mathbf{W}_\mu^a$  ( $a = 1, 2, 3$ ) and  $\mathbf{B}_\mu$  are the gauge fields.

The gauge fields  $\mathbf{W}_\mu^a$  and  $\mathbf{B}_\mu$  transform under the  $SU(2)_L \otimes U(1)_Y$  symmetry as

$$\mathbf{W}_\mu^a \rightarrow \mathbf{W}_\mu^a - \frac{1}{g_W} \partial_\mu \alpha^a(x) - \epsilon^{abc} \alpha^b(x) \mathbf{W}_\mu^c \quad (2.17)$$

$$\mathbf{B}_\mu \rightarrow \mathbf{B}_\mu - \frac{1}{g_Y} \partial_\mu \beta(x) \quad (2.18)$$

where  $\epsilon^{abc}$  is the Levi-Civita tensor. The Lagrangian density of the electroweak is given by

$$\mathcal{L}_{EW} = \bar{\psi}_L (i\gamma^\mu D_\mu - m) \psi_L + \bar{\psi}_R (i\gamma^\mu D_\mu - m) \psi_R - \frac{1}{4} \mathbf{W}_{\mu\nu}^a \mathbf{W}_a^{\mu\nu} - \frac{1}{4} \mathbf{B}_{\mu\nu} \mathbf{B}^{\mu\nu} \quad (2.19)$$

---

<sup>3</sup> $\gamma^5$  is the product of the four gamma matrices.  $\gamma^5 = i\gamma^0\gamma^1\gamma^2\gamma^3 = \begin{pmatrix} 0 & 0 & 1 & 0 \\ 0 & 0 & 0 & 1 \\ 1 & 0 & 0 & 0 \\ 0 & 1 & 0 & 0 \end{pmatrix}$

<sup>4</sup>The left-handed fermion state  $\psi_L$  is a doublet.

<sup>5</sup>The Pauli matrices are  $\sigma_1 = \begin{pmatrix} 0 & 1 \\ 1 & 0 \end{pmatrix}$ ,  $\sigma_2 = \begin{pmatrix} 0 & -i \\ i & 0 \end{pmatrix}$ , and  $\sigma_3 = \begin{pmatrix} 1 & 0 \\ 0 & -1 \end{pmatrix}$

where  $\mathbf{W}_{\mu\nu}^a$  and  $\mathbf{B}_{\mu\nu}$  are the field strength tensors

$$\mathbf{W}_{\mu\nu}^a = \partial_\mu \mathbf{W}_\nu^a - \partial_\nu \mathbf{W}_\mu^a - g_W \epsilon^{abc} \mathbf{W}_\mu^b \mathbf{W}_\nu^c \quad (2.20)$$

$$\mathbf{B}_{\mu\nu} = \partial_\mu \mathbf{B}_\nu - \partial_\nu \mathbf{B}_\mu \quad (2.21)$$

and  $\bar{\psi} \equiv \psi^\dagger \gamma^0$  is the adjoint spinor of  $\psi$ <sup>6</sup>. Therefore, the mass eigenstates are the mixture of the gauge fields

$$\mathbf{W}_\mu^\pm = \frac{1}{\sqrt{2}}(\mathbf{W}_\mu^1 \mp i\mathbf{W}_\mu^2) \quad (2.22)$$

$$\begin{pmatrix} \mathbf{A}_\mu \\ \mathbf{Z}_\mu \end{pmatrix} = \begin{pmatrix} \cos \theta_W & \sin \theta_W \\ -\sin \theta_W & \cos \theta_W \end{pmatrix} \begin{pmatrix} \mathbf{B}_\mu \\ \mathbf{W}_\mu^3 \end{pmatrix}. \quad (2.23)$$

Thus, the mass eigenstates  $\mathbf{A}_\mu$ ,  $\mathbf{W}_\mu^\pm$ , and  $\mathbf{Z}_\mu$  are identified as the photon,  $\gamma$ ,  $W^\pm$  and  $Z^0$  bosons experimentally. The *Weinberg weak mixing angle*  $\theta_W$  is defined as

$$\tan \theta_W = \frac{g_Y}{g_W}. \quad (2.24)$$

The coupling constants  $g_W$  and  $g_Y$  are related to the electric charge by

$$e = g_W \sin \theta_W = g_Y \cos \theta_Y. \quad (2.25)$$

And the weak eigenstates of quark,  $q'$ , are the linear combinations of the mass eigenstates of quark,  $q$ , by the *Cabbibo-Kobayashi-Maskawa* (CKM) matrix [33]

$$\begin{pmatrix} d' \\ s' \\ b' \end{pmatrix} = \begin{pmatrix} V_{ud} & V_{us} & V_{ub} \\ V_{cd} & V_{cs} & V_{cb} \\ V_{td} & V_{ts} & V_{tb} \end{pmatrix} \begin{pmatrix} d \\ s \\ b \end{pmatrix}. \quad (2.26)$$

The CKM matrix allows the quarks changing their flavour and generation as observed in the experiment. Similarly, the *Pontecorvo-Maki-Nakagawa-Sakata* (PMNS) matrix [34] is responsible for the flavour changing of the neutrinos.

---

<sup>6</sup> $\psi^\dagger$  is the hermitian conjugate of  $\psi$

## Spontaneous symmetry breaking and Higgs mechanism

The gauge bosons of the weak interaction,  $W^\pm$  and  $Z^0$ , are massive particles<sup>7</sup>. However, the existence of the mass terms violate the gauge invariance of the  $\mathcal{L}_{EW}$ . In order to explain the mass of gauge bosons, the Englert-Brout-Higgs mechanism [35, 36, 37, 38, 39] was proposed in 1964. A new scalar complex  $SU(2)_L$  doublet field  $\Phi$  is introduced in the Higgs mechanism

$$\Phi = \begin{pmatrix} \Phi^+ \\ \Phi^0 \end{pmatrix} = \begin{pmatrix} \Phi_1 & i\Phi_2 \\ \Phi_3 & i\Phi_4 \end{pmatrix} \quad (2.27)$$

with hypercharge  $Y = 1$  and four degrees of freedom,  $\Phi_i$ , which are scalar fields and called the *Goldstone modes*. The Lagrangian density for this new field, Higgs field, is

$$\mathcal{L}_\Phi = (D^\mu \Phi)^\dagger (D_\mu \Phi) - V(\Phi) \quad (2.28)$$

where the Higgs potential is defined as

$$V(\Phi) = \mu^2 |\Phi|^2 + \lambda |\Phi|^4 \quad (2.29)$$

where  $\mu$  and  $\lambda$  are free parameters. The Higgs potential is shown in Figure 2.1. The Higgs potential is the rotation  $U(1)$  symmetry. Choosing any of the points at the bottom of the Higgs potential breaks the symmetry spontaneously. The *spontaneously symmetry breaking* (SSB) means the Lagrangian keeps invariant under certain symmetry but no longer invariant at the ground state.

Because the Higgs potential is invariant under  $SU(2)_L \otimes U(1)_Y$ , the parameters  $\mu$  and  $\lambda$  must satisfy  $\mu^2 < 0$  and  $\lambda > 0$  resulting in a set of degenerate ground states where  $\langle 0|\Phi|0\rangle \neq 0$ . Among the degenerate ground states, the ground state is often chosen to

---

<sup>7</sup> $m_W = 80.385 \pm 0.015$  GeV and  $m_Z = 91.1876 \pm 0.0021$  GeV



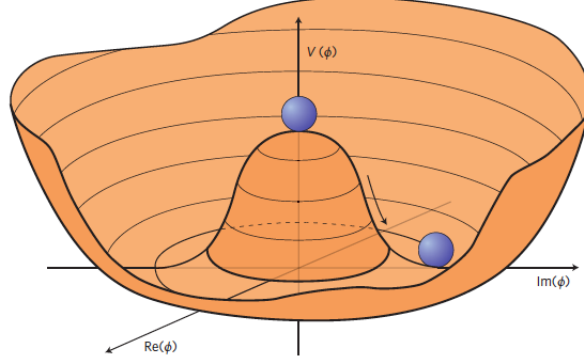


**Figure 2.1:** An illustration of the Higgs potential which has the form of a Mexican hat. The figure is taken from [40].

have the form

$$\Phi = \frac{1}{\sqrt{2}} \begin{pmatrix} 0 \\ v \end{pmatrix} \quad (2.30)$$

where  $v = \sqrt{-\mu^2/\lambda}$  is the *vacuum expectation value* (VEV). This particular choice of the ground state breaks the  $SU(2)_L \otimes U(1)_Y$  symmetries spontaneously and ensures the unbroken electromagnetic interaction under  $U(1)_{EM}$  symmetry and photon being massless. By introducing a massive particle, Higgs boson  $H$ , the Higgs field can be re-written as

$$\Phi = \frac{1}{\sqrt{2}} \begin{pmatrix} 0 \\ v + H \end{pmatrix} \quad (2.31)$$

and the kinematic term of the Lagrangian density becomes

$$\mathcal{L}_\Phi^{\text{kinematic}} = (D^\mu \Phi)^\dagger (D_\mu \Phi) \quad (2.32)$$

$$= \frac{1}{2} \partial_\mu H \partial^\mu H + (v + H)^2 \left\{ \frac{g_W^2}{4} \mathbf{W}_\mu^\dagger \mathbf{W}^\mu + \frac{g_W^2}{8 \cos^2 \theta_W} \mathbf{Z}_\mu^\dagger \mathbf{Z}^\mu \right\} \quad (2.33)$$

and the Higgs potential is now

$$V(\Phi) = -\frac{v^2 \lambda}{2} (v + H)^2 + \frac{\lambda}{4} (v + H)^4. \quad (2.34)$$

Thus the masses of the  $W^\pm$  and  $Z^0$  are obtained by the interaction between the gauge

bosons and Higgs boson. The masses are defined as

$$m_H = v\sqrt{2\lambda}, \quad m_W = \frac{v}{2}g_W, \quad m_Z = \frac{v}{2}\sqrt{g_W^2 + g_Y^2}, \quad m_\gamma = 0. \quad (2.35)$$

However, the masses of fermions are obtained by the *Yukawa interaction*

$$\mathcal{L}_{\text{Yukawa}} = y_f \bar{L}_L \Phi f_R + y_f \bar{Q}_L \Phi f_R + \text{h.c.} \quad (2.36)$$

where the  $y_f$  is *Yukawa coupling*,  $f$  stands for  $\{\ell^i, u^i, d^i\}$  and h.c. represents the hermitian conjugate, respectively. The  $\bar{L}_L$  and  $\bar{Q}_L$  are the left-handed lepton and quark doublet and  $f_R$  is the lepton or quark singlet. The mass of fermion is defined as

$$m_f = \frac{v}{\sqrt{2}} y_f \quad (2.37)$$

where  $y_f$  is a free parameter which causes the fermion mass not predictable. Finally, the non-zero VEV,  $v$ , can be related to *Fermi constant*,  $G_F$ , by

$$v = \frac{1}{\sqrt{\sqrt{2}G_F}} \approx 246 \text{ GeV}. \quad (2.38)$$

### 2.1.5 The discovery of Higgs boson

A lot of the SM predictions are successfully confirmed by the experimental observations besides the existence of the theoretical Higgs boson. The search of the Higgs boson has become a major goal of the experimental particle physicists. A Higgs-like resonance was discovered and announced on July 4th 2012 by the ATLAS<sup>8</sup> and CMS<sup>9</sup> collaborations [1, 2]. By combining the data with integrated luminosities of  $4.8 \text{ fb}^{-1}$  collected at  $\sqrt{s} = 7 \text{ TeV}$  in 2011 and  $5.8 \text{ fb}^{-1}$  at  $\sqrt{s} = 8 \text{ TeV}$  in 2012, the ATLAS experiment measured the mass of the Higgs boson to be  $126.0 \pm 0.4 \text{ (stat.)} \pm 0.4 \text{ (syst.) GeV}$  with significance of  $5.9\sigma$  corresponding to a background fluctuation probability of  $1.7 \times 10^{-9}$  [1]. In the meantime,

---

<sup>8</sup>A Toroidal LHC ApparatuS

<sup>9</sup>Compact Muon Solenoid

the CMS experiment announced the mass of the Higgs boson to be  $125.3 \pm 0.4$  (stat)  $\pm 0.5$  (syst.) GeV with significance  $5.0\sigma$  using integrated luminosities of up to  $5.1 \text{ fb}^{-1}$  at 7 TeV and  $5.3 \text{ fb}^{-1}$  at 8 TeV [2]. The  $H \rightarrow ZZ^{(*)} \rightarrow 4\ell$ ,  $H \rightarrow \gamma\gamma$ , and  $H \rightarrow WW^{(*)} \rightarrow e\nu\mu\nu$  channels were studied by the ATLAS collaboration and the  $H \rightarrow \gamma\gamma, ZZ, W^+W^-, \tau^+\tau^-,$  and  $b\bar{b}$  channels were studied by the CMS collaboration. In the Figure 2.2 shows the local  $p$ -value as a function of the Higgs mass for ATLAS and CMS results, respectively.

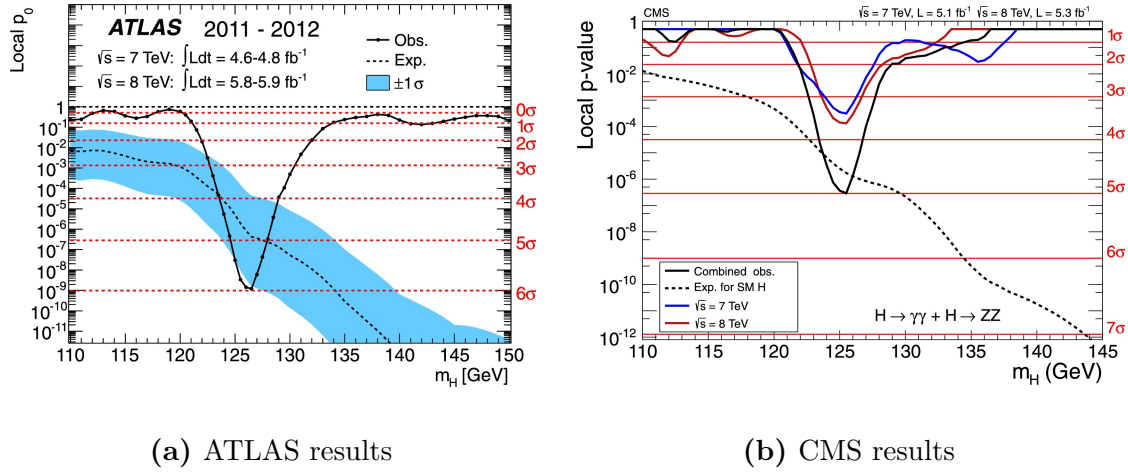


**Figure 2.2:** The observed local  $p$ -value as a function of  $m_H$  for the ATLAS [1] and CMS [2] experiment, respectively. The dashed line shows the expected local  $p_0$  for a SM Higgs boson. The horizontal lines denotes the  $p$ -values corresponding to significances of 1 to  $6\sigma$ .

## 2.2 Beyond the Standard Model

Although the SM is an incredible successful theory for explaining the phenomenon in the particle physics, it leaves some questions which can no be answered. Some of the unanswered questions are introduced in the rest part of this section.

### 2.2.1 Hierarchy problem

The weakest force in the SM is the weak force but the strength of the weak force is  $10^{24}$  times as strong as gravitational force which doesn't incorporate into the SM. The large discrepancy between the weak force and the gravitational force is called the hierarchy problem [9, 41, 42]. The classical potential of the SM Higgs field  $\Phi$  is

$$V(\Phi) = \mu^2 |\Phi|^2 + \lambda |\Phi|^4. \quad (2.39)$$

Since the SM requires the VEV for  $\Phi$ ,  $\langle \Phi \rangle$ , at the minimum of the potential non-vanishing, this is only satisfied if  $\mu^2 < 0$  and  $\lambda > 0$ . However, the parameter  $\mu^2$  receives enormous radiative corrections causing it to be ultraviolet divergent as shown in Equation 2.40.

$$\mu^2 = \mu_{bare}^2 - \frac{|\lambda_f|^2}{8\pi} \Lambda_{UV}^2 + \mathcal{O}(\Lambda_{UV}^2) \quad (2.40)$$

where  $\mu_{bare}$  is the Higgs mass,  $-\frac{|\lambda_f|^2}{8\pi} \Lambda_{UV}^2$  is the one-loop correction, and  $\Lambda_{UV}$  is an ultraviolet momentum cutoff which is valid up to the Planck scale  $10^{19}$  GeV. The electroweak gauge bosons  $W^\pm$  and  $Z^0$  obtain their finite masses from  $\langle \Phi \rangle$  so the  $\mu^2$  cannot be divergent. There must be some unknown mechanism to protect from divergence.

### 2.2.2 Dark matter and dark energy

The matters we know today compose of only 5% [43, 44] of the content of the universe and the remaining part is something we don't know. This unknown matter is called *Dark Matter* (DM) [45] which makes up about 27% of the universe and the rest 68% are called *Dark Energy* (DE) [43, 44]. Because DM interacts weakly and doesn't interact with the electromagnetic force, it doesn't absorb, emit, or reflect light causing it hard to detect directly. The name DM comes from it is invisible. Dark energy distributes evenly in both space and time throughout the universe so it doesn't dilute when the universe

expands. The observed scientific data hints the presence of DE is necessary to explain the accelerated expansion of the universe.

### 2.2.3 Grand Unification

Maxwell unified the electricity and magnetism into electromagnetism in the 1860s. About a century later, physicists successfully developed theory of electroweak which links the electromagnetism and the weak force. Because of the triumph of electroweak theory, theorists raise the question of the possibility to unify all forces. The *Grand Unified Theory* (GUT) [46], which tries to link three of the four known forces together, is developed in the mid-1970s by theorists. The GUT proposes that the electromagnetic force, weak force, and strong force unify to one force at the GUT scale,  $\Lambda_{GUT} \approx 10^{16}$  GeV. So the three running coupling constants [47] are expected to be converged at the GUT scale. However, the current experiment results show the coupling constants still different as shown in Figure 2.3.

### 2.2.4 More questions

There are some more interesting questions which we don't know the answers. For example, we don't know the reason why there are 61 elementary particles and more than 20 arbitrary parameters in the SM. Also, the SM doesn't explain why there are only three generations. The amount of matter and anti-matter are equal at the beginning of the universe based on the prediction of the SM but the matter dominates in the currently universe which the SM couldn't answer the reason why.

In order to answer these questions, there are many theories being developed on the top of SM but none of them has been observed. One of the most probable candidate for

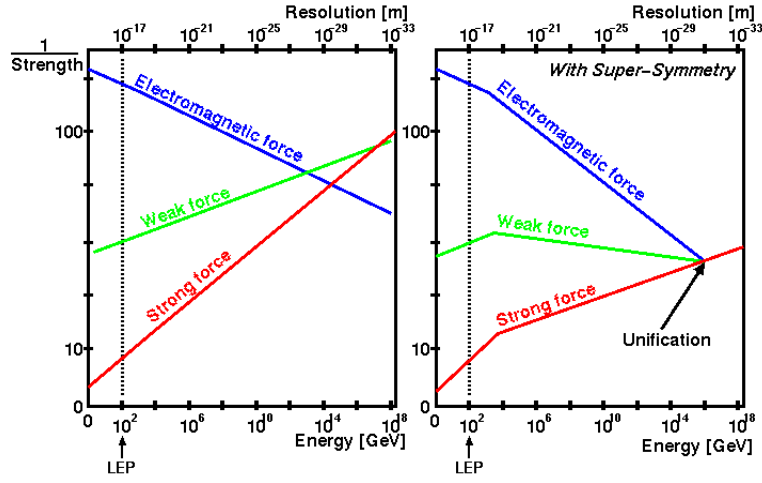


**Figure 2.3:** The measured running coupling constants in the SM (left) and prediction in the GUT (right). The three lines show the inverse value of the coupling constant for the three fundamental forces. This figure is taken from [48].

answering these question is supersymmetry which will be introduced in the next chapter.

# Chapter 3

## Supersymmetry

The SM [23, 24, 25, 26, 27] gets a stupendous success in expecting and explaining the physics phenomena of the elementary particles. However, the SM leaves several open questions unanswered as mentioned in Section 2.2. Many different models of new physics were proposed to explain those unanswered questions. Among these new models, the *supersymmetry* (SUSY) [49, 50, 51, 9, 52, 53, 54, 55, 56] wins most physicists' favour. The SUSY proposed by Wess and Zumino [49] at early 1970s is a symmetry relating bosonic and fermionic degrees of freedom. It extends the SM by requiring every SM boson/fermion has a fermionic/bosonic supersymmetric partner and vice versa. The reason why physicists favour SUSY is described in Section 3.1 and the introduction of the SUSY as well as the formulaism are given in Section 3.2. The *Radiative Natural SUSY* (RNS) and the *Non-Universal Higgs Mass model* with two extra parameters (NUHM2) are given in Section 3.3 and 3.4, respectively.

### 3.1 Why supersymmetry

The SM leaves several unanswered questions, for example, the hierarchy problem (Section 2.2.1), what is the candidates of dark matter (Section 2.2.2), and why don't the

running coupling constants unify at GUT level (Section 2.2.3). The SUSY provides good explanations for these questions.

### Hierarchy problem

The SM expects the Higgs squared mass divergent at the Plank scale  $\sim 10^{19}$  GeV. However, the  $W^\pm$  and  $Z^0$  gauge bosons obtained their finite mass through the Higgs mechanism indicates the Higgs squared mass must be finite. The Figure 3.1 shows the Feymann diagram for the one loop correction to the Higgs squared mass due to a fermion  $f$  and a scalar  $S$ .



**Figure 3.1:** The Feymann diagram for the one loop correction to the Higgs squared mass due to (a) a fermion  $f$  and (b) a scalar  $S$ . The figure is taken from [9].

The corrections are

$$\Delta m_H^2 = -\frac{|\lambda_f^2|}{8\pi^2} \Lambda_{UV}^2 + \dots, \quad \text{fermion} \quad (3.1)$$

$$\Delta m_H^2 = \frac{\lambda_S}{16\pi^2} \Lambda_{UV}^2 + \dots, \quad \text{boson} \quad (3.2)$$

where the  $\Lambda_{UV}$  is an ultraviolet momentum cutoff which is valid up to the Plank scale  $10^{19}$  GeV. The corrections diverge when  $\Lambda_{UV}$  becoming very large. Because the contributions from the fermion and scalar loops have opposite sign, the divergence contributions can be canceled out if there is a scalar loop for each fermionic loop. The SUSY predicts



the existence of the bosonic/fermionic sparticles, therefore, if  $\lambda_S = 2|\lambda_f^2|$  then the SUSY maintain the finiteness of the Higgs squared mass in a natural way.

## Dark matter

The dark matter (DM) makes up about 27% of the universe and it might originate from neutral relic from the early universe. The cosmology observations of the DM indicate that the dark matter should be electrically neutral, cold, massive, and it participates only the weak and gravitational interactions. Therefore, the DM candidate should be a new particle which is *weakly interacting massive particle* (WIMP). The SUSY requires all the sparticles must be produced in pairs and they decay into stable *lightest SUSY particles* (LSP) with odd number. If there are a lot of sparticles produced in the early Universe, they will have to decayed to LSPs and remain until the present day because the LSP is stable. The LSP is a weakly interacting massive particle. It doesn't interact electromagnetically so they cannot be scattered by photon and thus dark. There are 3 kinds of LSP could be the possible DM candidate, the lightest *neutralino*, the lightest *sneutrino* and the *gravitino*.

## Grand Unification

The Grand Unified Theory (GUT) tries to unify the strong and electroweak interactions. There will be only one interaction and one coupling constant at the GUT scale ( $\approx 10^{16}$  GeV). However, the current coupling constants for electromagnetic, weak, and strong interactions don't unified at the GUT scale as shown in the left hand side of Figure 2.3. This problem can be solved by introducing the SUSY which modifies the renormalization group equations and make the running gauge couplings converged at the GUT scale. The right hand side of Figure 2.3 shows the running gauge couplings in SUSY.

## 3.2 Introduction of the supersymmetry

An brief overview of the SUSY are introduced in this section. Firstly, the mathematical foundation of the SUSY, superalgebra, is described in Section 3.2.1 followed by the superspace and superfields in Section 3.2.2.

### 3.2.1 Superalgebra

#### Poincaré algebra

The SUSY is based on the superalgebra which is an extension of space-time Poincaré algebra. The Poincaré group is a product of the Lorentz group and the group of translations in space-time. A Lorentz group must satisfies the commutation relations

$$[J_i^+, J_j^+] = i\epsilon_{ijk}J_k^+, \quad [J_i^-, J_j^-] = i\epsilon_{ijk}J_k^-, \quad [J_i^+, J_j^-] = 0 \quad (3.3)$$

where  $i, j, k = 1, 2, 3$ . If the six Lorentz group generators are combined into an antisymmetric second rank tensor generator  $M_{\mu\nu}$  where  $M_{ij} = \epsilon_{ijk}J_k$  and  $M_{0i} = -M_{i0} = -K_i$ <sup>1</sup> and the generator of the translation groups is  $P_\mu$ , the energy-momentum operator, then the commutation relations of the Poincaré group are

$$[P_\mu, P_\nu] = 0, \quad (3.4)$$

$$[M_{\mu\nu}, P_\lambda] = i(g_{\nu\lambda}P_\mu - g_{\mu\lambda}P_\nu), \quad (3.5)$$

$$[M_{\mu\nu}, M_{\rho\sigma}] = -i(g_{\mu\rho}M_{\nu\sigma} - g_{\mu\sigma}M_{\nu\rho} - g_{\nu\rho}M_{\mu\sigma} + g_{\nu\sigma}M_{\mu\rho}). \quad (3.6)$$

---

<sup>1</sup>The  $J_i$  and  $K_i$  with  $i = 1, 2, 3$  are rotation and boost generators in 3-dimension respectively. And the ladder operators are defined as  $J_i^\pm = \frac{1}{2}(J_i \pm iK_i)$ .

where the metric is

$$g_{\mu\nu} = \begin{pmatrix} 1 & 0 & 0 & 0 \\ 0 & -1 & 0 & 0 \\ 0 & 0 & -1 & 0 \\ 0 & 0 & 0 & -1 \end{pmatrix} \quad (3.7)$$

## Spinor

A general spin  $\frac{1}{2}$  particle state,  $\chi$ , can be expressed as a *spinor* in the SUSY using two-component spin up  $\chi_+$  and spin down  $\chi_-$  column matrices

$$\chi = c_+ \chi_+ + c_- \chi_- = c_+ \begin{pmatrix} 1 \\ 0 \end{pmatrix} + c_- \begin{pmatrix} 0 \\ 1 \end{pmatrix} = \begin{pmatrix} c_+ \\ c_- \end{pmatrix} \quad (3.8)$$

The solution of the Dirac equation<sup>2</sup>,  $\psi_D$ <sup>3</sup>, can be expressed using the left-handed and right-handed *Weyl spinors*  $\psi_L$  and  $\psi_R$

$$\psi_D = \begin{pmatrix} \psi_1 \\ \psi_2 \\ \psi_3 \\ \psi_4 \end{pmatrix} = \begin{pmatrix} \begin{pmatrix} \psi_1 \\ \psi_2 \end{pmatrix} \\ \begin{pmatrix} \psi_3 \\ \psi_4 \end{pmatrix} \end{pmatrix} = \begin{pmatrix} \psi_L \\ \psi_R \end{pmatrix} \quad (3.9)$$

It is convenient to use the Weyl spinors to represent the building blocks for any fermion field. The Majorana spinor  $\tilde{\psi}_M$  is a real solution of Dirac equation. It is its own charge conjugate and satisfies the Majorana condition

$$\tilde{\psi}_M = \tilde{\psi}_M^* \quad (3.10)$$

The Majorana spinor can be expressed in terms of the Weyl spinors

$$\psi_M = \begin{pmatrix} \xi_\alpha \\ \bar{\xi}^{\dot{\alpha}} \end{pmatrix} \quad (3.11)$$

---

<sup>2</sup>The Dirac equation is  $(i\gamma^\mu \partial_\mu - m)\psi = 0$ .

<sup>3</sup>The Dirac spinor  $\psi_D$  is a four-component field which can be expressed using a four-component matrix.

where the left-handed Weyl spinor  $\xi_\alpha$  and the right-handed Weyl spinor  $\bar{\xi}^{\dot{\alpha}}$  are the Hermitian conjugate of each other.

## Helicity

A particle with momentum  $\vec{p}$  and angular momentum  $\vec{J}$ , then the *helicity* is defined as

$$h = \vec{J} \cdot \hat{p} = (\vec{L} + \vec{S}) \cdot \hat{p} = \vec{S} \cdot \hat{p}, \quad \hat{p} = \frac{\vec{p}}{|\vec{p}|} \quad (3.12)$$

The eigenvalues of  $h$  are +1 and -1 corresponding to right-handed and left-handed eigenstates. Although the helicity is rotation invariant but not boost invariant, the helicity of a massless particle moving at the speed of light is Lorentz invariant.

### 3.2.2 Superspace and superfields

The superspace is composed of the ordinary space-time coordinate and four anticommuting fermionic coordinates  $\theta_\alpha$  and  $\bar{\theta}_{\dot{\alpha}}$  where the spinor indices  $\alpha$  and  $\dot{\alpha}$  can be 1 or 2. A superfield  $S(x^\mu, \theta_\alpha, \bar{\theta}_{\dot{\alpha}})$  is a function in superspace. The general form of a superfield can be expressed in terms of  $\theta$  and  $\bar{\theta}$

$$S(x, \theta, \bar{\theta}) = a + \theta\xi + \bar{\theta}\bar{\chi} + \theta\theta b + \bar{\theta}\bar{\theta}c + \bar{\theta}\bar{\sigma}^\mu\theta v_\mu + \theta\theta\bar{\theta}\bar{\zeta} + \bar{\theta}\bar{\theta}\theta\eta + \theta\theta\bar{\theta}\bar{\theta}d \quad (3.13)$$

where all spinor indices are suppressed. The  $a, b, c, d$ , and  $v_\mu$  are bosonic fields and  $\xi, \bar{\chi}, \bar{\zeta}, \eta$  are fermionic fields which are complex functions of  $x^\mu$ . The SUSY generators  $Q_\alpha$  and  $\bar{Q}_{\dot{\alpha}}$  can be expressed as

$$Q_\alpha = -i\frac{\partial}{\partial\theta^\alpha} - \sigma_{\alpha\dot{\beta}}^\mu\bar{\theta}^{\dot{\beta}}\partial_\mu, \quad \bar{Q}_{\dot{\alpha}} = i\frac{\partial}{\partial\bar{\theta}^{\dot{\alpha}}} + \theta^\beta\sigma_{\beta\dot{\alpha}}^\mu\partial_\mu \quad (3.14)$$

and the commutation relations are

$$\{Q_\alpha, \bar{Q}_{\dot{\beta}}\} = -2i\sigma_{\alpha\dot{\beta}}^\mu\partial_\mu, \quad \{Q_\alpha, Q_\beta\} = \{\bar{Q}_{\dot{\alpha}}, \bar{Q}_{\dot{\beta}}\} = 0 \quad (3.15)$$

The SUSY covariant derivatives are defined as

$$D_\alpha = \frac{\partial}{\partial \theta^\alpha} + i\sigma^\mu_{\alpha\dot{\beta}} \bar{\theta}^{\dot{\beta}} \partial_\mu, \quad \bar{D}_{\dot{\alpha}} = (D_\alpha)^\dagger = \frac{\partial}{\partial \bar{\theta}^{\dot{\alpha}}} + i\theta^\beta \sigma^\mu_{\beta\dot{\alpha}} \partial_\mu \quad (3.16)$$

and the commutation relations are

$$\{D_\alpha, \bar{D}_{\dot{\beta}}\} = 2i\sigma^\mu_{\alpha\dot{\beta}} \partial_\mu, \quad \{D_\alpha, D_\beta\} = \{\bar{D}_{\dot{\alpha}}, \bar{D}_{\dot{\beta}}\} = 0 \quad (3.17)$$

The SUSY covariant derivatives anticommute with the SUSY generators<sup>4</sup>.

### Chiral superfields and vector superfields

The spin 0 bosons and spin 1/2 fermions are described using the *chiral superfield* and the spin 1 gauge bosons are described using the *vector superfields*.  $V(x, \theta, \bar{\theta})$ . The chiral superfield,  $\Phi(x, \theta, \bar{\theta})$ , satisfies the condition<sup>5</sup>

$$\bar{D}_{\dot{\alpha}} \Phi = 0 \quad (3.18)$$

If we redefine the new coordinates  $(y^\mu, \theta)$  and  $(\bar{y}^\mu, \bar{\theta})$  in the surface<sup>6</sup>,

$$y^\mu = x^\mu + i\theta\sigma^\mu\bar{\theta}, \quad \bar{y}^\mu = x^\mu - i\theta\sigma^\mu\bar{\theta} \quad (3.19)$$

then the covariant derivatives become

$$D_\alpha = \frac{\partial}{\partial \theta^\alpha} + 2i\sigma^\mu_{\alpha\dot{\beta}} \bar{\theta}^{\dot{\beta}} \frac{\partial}{\partial y^\mu}, \quad \bar{D}_{\dot{\alpha}} = \frac{\partial}{\partial \bar{\theta}^{\dot{\alpha}}} \quad (3.20)$$

And the general form of a chiral superfield can be expressed in terms of the chiral coordinate  $(y^\mu, \theta)$  only

$$\Phi(y, \theta) = \phi(y) + \sqrt{2}\theta\psi(y) + \theta\theta F(y) \quad (3.21)$$

---

<sup>4</sup> $\{D_\alpha, Q_\beta\} = \{D_\alpha, \bar{Q}_{\dot{\beta}}\} = \{\bar{D}_{\dot{\alpha}}, Q_\beta\} = \{\bar{D}_{\dot{\alpha}}, \bar{Q}_{\dot{\beta}}\} = 0$

<sup>5</sup>The antichiral superfield satisfies  $D_\alpha \Phi^* = 0$  where  $\Phi^*$  is the complex conjugate of  $\Phi$ .

<sup>6</sup>The chiral coordinate is  $(y^\mu, \theta)$  and the antichiral coordinate is  $(\bar{y}^\mu, \bar{\theta})$

The vector superfield,  $V$ , is a real field<sup>7</sup> and the general form is

$$V(x, \theta, \bar{\theta}) = C + i\theta\chi - i\bar{\theta}\bar{\chi} + \theta\sigma^\mu\bar{\theta}v_\mu + \frac{i}{2}\theta\theta(M + iN) - \frac{i}{2}\bar{\theta}\bar{\theta}(M - iN) \quad (3.22)$$

$$+ i\theta\theta\bar{\theta}(\bar{\lambda} + \frac{i}{2}\bar{\sigma}^\mu\partial_\mu\chi) - i\bar{\theta}\bar{\theta}\theta(\lambda - \frac{i}{2}\sigma^\mu\partial_\mu\bar{\chi}) + \frac{1}{2}\theta\theta\bar{\theta}\bar{\theta}(D - \frac{1}{2}\partial^2 C) \quad (3.23)$$

where the  $C, M, N, D$  are real scalars, the  $\chi, \lambda$  are Weyl spinors, and the  $v_\mu$  is a vector field. By applying the Wess-Zumino gauge, the general form can be reduced into

$$V_{WZ} = \theta\sigma^\mu\bar{\theta}v_\mu + i\theta\theta\bar{\theta}\bar{\lambda} - i\bar{\theta}\bar{\theta}\theta\lambda + \frac{1}{2}\theta\theta\bar{\theta}\bar{\theta}D \quad (3.24)$$

The non-vanishing power of  $V_{WZ}$  is  $V_{WZ}^2 = \frac{1}{2}\theta\theta\bar{\theta}\bar{\theta}v_\mu v^\mu$ . All the higher power of  $V_{WZ}$  are all vanishing  $V_{WZ}^n = 0, n \geq 3$ .

### 3.2.3 $R$ -parity

The baryon number  $B$  and lepton number  $L$  are conserved in the SM but violated in the SUSY. Therefore, a new symmetry called  $R$ -parity is introduced to eliminate the  $B$  and  $L$  violating term. The  $R$ -parity is defined as

$$R \equiv (-1)^{3(B-L)+2s} \quad (3.25)$$

where  $s$  is the spin of the particle. All of the SM particles have even  $R$ -parity ( $R = +1$ ), while all of the sparticles have odd  $R$ -parity ( $R = -1$ ). If the  $R$ -parity is conserved, SUSY predicts that sparticles are produced in pairs in collider experiments.

### 3.2.4 Supersymmetry breaking

The supermultiplets are the single particle states in SUSY theory and it corresponds to the irreducible representations of the super-Poincaré algebra. A supermultiplet contains boson

---

<sup>7</sup>The vector superfield satisfies  $V(x, \theta, \bar{\theta}) = V^\dagger(x, \theta, \bar{\theta})$ .

and fermion with the same degrees of freedom and all particles in the same supermultiplet have the same mass. However, no any sparticles have been observed from the experiments. Therefore, the SUSY must be spontaneously broken and the sparticles must be heavier than their SM partners. The scalar superpotential  $V$  can be represented by the auxiliary fields  $F_i$  and  $D_a$

$$V = F^{*i}F_i + \frac{1}{2} \sum_a D^a D_a \quad (3.26)$$

A state  $|\Omega\rangle$  is called a vacuum state if  $E_\Omega = \langle\Omega|H|\Omega\rangle = 0$ . This happens when the potential  $V$  has a minimum. There are two kinds of vacuums, the true vacuum and the false vacuum which correspond to the global minimum and the local minimum of the scalar potential  $V$ , respectively. For example, when  $F_i = D_a = 0$ , then  $V = 0$  is a global minimum. The  $\langle F \rangle = 0$  is called  $F$ -term breaking and the  $\langle D \rangle = 0$  is called  $D$ -term breaking.

### 3.2.5 The Minimal Supersymmetry Standard Model

The Minimal Supersymmetry Standard Model (MSSM) is the minimal extension of the Standard Model. The MSSM contains only the smallest number of superfields and interactions such that the SM particles can keep their current forms.

#### Particle content

All the super particles, *sparticles*<sup>8</sup>, have exactly the same quantum number as their SM particles except the spins differ by  $\frac{1}{2}$ . The super partners of the leptons and quarks are called *sleptons* and *squarks*. The sleptons and squarks are scalar particles with spin  $s = 0$  and the left-handed and right-handed states are treated as different particles such that

---

<sup>8</sup>The super particles of the SM fermions are prefix a "s" and the super particles of the SM bosons are suffix an "ino". A tilde is added on the symbol of the SM particle to denote its super partner.

the SM particles and the SUSY sparticles have the same number of degree of freedom. The super partners of gluons are *gluinos* and there are eight gluinos with spin  $s = \frac{1}{2}$ . The super partners of the gauge bosons  $W^\pm, Z^0$ , and  $\gamma$ , are *gauginos*. The gauginos have spin  $s = \frac{1}{2}$ . The super partners of the Higgs bosons<sup>9</sup> are *Higgsinos*. The Higgsinos and gauginos mixing states are two *charginos*  $\tilde{\chi}_1^\pm, \tilde{\chi}_2^\pm$  and four *neutralinos*  $\tilde{\chi}_1^0, \tilde{\chi}_2^0, \tilde{\chi}_3^0, \tilde{\chi}_4^0$  with spin  $s = \frac{1}{2}$ . Table 3.1 shows the particle contents in the MSSM.

Supermultiplet	Names	Symbol	spin 0	spin 1/2	spin 1	$SU(3)_C \otimes SU(2)_L \otimes U(1)_Y$
Chiral	squarks, quarks ( $\times 3$ families)	Q	$(\tilde{u}_L, \tilde{d}_L)$	$(u_L, d_L)$	-	$\mathbf{3} \otimes \mathbf{2} \otimes \frac{1}{6}$
		$\bar{u}$	$\tilde{u}_R^*$	$u_R^\dagger$	-	$\bar{\mathbf{3}} \otimes \mathbf{1} \otimes -\frac{2}{3}$
		$\bar{d}$	$\tilde{d}_R^*$	$d_R^\dagger$	-	$\bar{\mathbf{3}} \otimes \mathbf{1} \otimes \frac{1}{3}$
Chiral	sleptons, leptons ( $\times 3$ families)	L	$(\tilde{\nu}, \tilde{e}_L)$	$(\nu, e_L)$	-	$\mathbf{1} \otimes \mathbf{2} \otimes -\frac{1}{2}$
		$\bar{e}$	$\tilde{e}_R^*$	$e_R^\dagger$	-	$\mathbf{1} \otimes \mathbf{1} \otimes 1$
Chiral	Higgs, higgsinos	$H_u$	$(H_u^+, H_u^0)$	$(\tilde{H}_u^+, \tilde{H}_u^0)$	-	$\mathbf{1} \otimes \mathbf{2} \otimes +\frac{1}{2}$
		$H_d$	$(H_d^0, H_d^-)$	$(\tilde{H}_d^0, \tilde{H}_d^-)$	-	$\mathbf{1} \otimes \mathbf{2} \otimes -\frac{1}{2}$
Gauge	gluino, gluon	-	-	$\tilde{g}$	$g$	$\mathbf{8} \otimes \mathbf{1} \otimes 0$
	winos, $W$ bosons	-	-	$\tilde{W}^\pm, \tilde{W}^0$	$W^\pm, W^0$	$\mathbf{1} \otimes \mathbf{3} \otimes 0$
	bino, $B$ boson	-	-	$\tilde{B}^0$	$B^0$	$\mathbf{1} \otimes \mathbf{1} \otimes 0$

**Table 3.1:** Chiral supermultiplets and gauge supermultiplets in the MSSM. In the chiral supermultiplets, the spin 0 fields are complex scalars and the spin 1/2 fields are left-handed two-component Weyl spinors.

### 3.3 The radiative natural SUSY

The radiative natural SUSY (RNS) [57, 58, 59, 60] is based on MSSM and it may be valid all the way up to the GUT scale<sup>10</sup>. The RNS maintains the Higgs mass  $m_h \sim 125$  GeV

<sup>9</sup>The Higgs sector contains two charged states  $H^\pm$  and three neutral states  $h^0, H^0$ , and  $A^0$ . The  $h^0$  and  $H^0$  are  $CP$  even state and  $A^0$  is  $CP$  odd state.

<sup>10</sup>The GUT scale is about  $M_{\text{GUT}} \approx 2 \times 10^{16}$  GeV.



and  $Z$  boson mass  $m_Z = 91.2$  GeV and requires no large cancellations at the electroweak scale. It also expects the light higgsino masses to be  $100 \sim 300$  GeV, the electroweak gaugino masses  $300 \sim 1200$  GeV, the masses of  $\tilde{g}$ ,  $\tilde{t}$ , and  $\tilde{b}$  to be  $1 \sim 4$  TeV, and the masses of  $\tilde{u}$ ,  $\tilde{d}$ ,  $\tilde{s}$ ,  $\tilde{c}$  exist in the  $5 \sim 30$  TeV range. In SUSY models, the  $Z$  boson mass can be obtained from the minimization condition on the Higgs sector scalar potential

$$\frac{m_Z^2}{2} = \frac{m_{H_d}^2 + \Sigma_d^d - (m_{H_u}^2 + \Sigma_u^u) \tan^2 \beta}{\tan^2 \beta - 1} - \mu^2 \quad (3.27)$$

where  $\Sigma_d^d$  and  $\Sigma_u^u$  are radiative corrections including the contributions from various particles and sparticles Yukawa and gauge couplings to the Higgs sector. Requiring no large cancellations means each term on the right-hand-side of Equation 3.27 are individually comparable to the left-hand-side,  $m_Z^2/2$ . Therefore, no large electroweak fine-tuning (EWFT) is required to obtain  $m_Z = 91.2$  GeV. The EWFT parameter is defined as

$$\Delta_{EW} = \max_i \frac{|C_i|}{(m_Z^2/2)} \quad (3.28)$$

which depends only on the weak scale parameters of the theory. Low  $\Delta_{EW}$  value means less fine-tuning. For example,  $\Delta_{EW} = 1 \sim 30$  correspond to  $3 \sim 15\%$  fine-tuning. The  $C_i$  represents  $C_{H_d}$ ,  $C_{H_u}$ ,  $C_\mu$ ,  $C_{\Sigma_d^d(k)}$ , and  $C_{\Sigma_u^u(k)}$

$$C_{H_d} = \frac{m_{H_d}^2}{\tan^2 \beta - 1} \quad (3.29)$$

$$C_{H_u} = \frac{-m_{H_u}^2 \tan^2 \beta}{\tan^2 \beta - 1} \quad (3.30)$$

$$C_\mu = -\mu^2 \quad (3.31)$$

$$C_{\Sigma_d^d(k)} = \frac{\Sigma_d^d}{\tan^2 \beta - 1} \quad (3.32)$$

$$C_{\Sigma_u^u(k)} = \frac{-\Sigma_u^u \tan^2 \beta}{\tan^2 \beta - 1} \quad (3.33)$$

where  $k$  denotes the various loop contributions included in Equation 3.27. In order to get a small EWFT value,  $\Delta_{EW} \leq 30$ , the RNS has to satisfy

- The light higgsino mass  $100 < |\mu| < 300$  GeV.
- $m_{H_u}(M_{\text{GUT}}) \sim (1.3 \sim 2)m_0$ . This leads to  $m_{H_u}^2 \sim -\frac{m_Z^2}{2}$  at the weak scale.
- $A_0 \sim \pm 1.6m_0$ . This results in large radiative corrections of  $\tilde{t}_i$  whilst maintain  $m_h$  to the  $\sim 125$  GeV.

In the RNS framework, the masses of the higgsino-like gauginos  $\tilde{\chi}_1^\pm$ ,  $\tilde{\chi}_1^0$ , and  $\tilde{\chi}_2^0$  lie in 100 to 300 GeV and the mass gap between  $\tilde{\chi}_2^0$  and  $\tilde{\chi}_1^0$  is  $10 \sim 30$  GeV. The masses of third generation squarks are  $m_{\tilde{t}_1} \sim 1$  to 2 TeV and  $m_{\tilde{t}_2}$ ,  $m_{\tilde{b}_1} \sim 2$  to 4 TeV. The gluino mass,  $m_{\tilde{g}}$ , is about 1 to 5 TeV and the masses of first and second generation sferminos,  $m_{\tilde{q}}, m_{\tilde{\ell}}$ , are about 5 to 10 TeV.

### 3.4 The non-universal Higgs model with two extra parameters

The RNS can be generated from SUSY GUT type models using non-universal Higgs masses model with two extra parameters (NUHM2) [61, 62, 63, 64] leading to a low fine-tuning  $\Delta_{EW}$  value at the electroweak scale and keeping electroweak naturalness. The NUHM2 decouples the mass parameters  $m_{H_u}^2$  and  $m_{H_d}^2$  at the GUT scale such that

$$m_{H_u}^2 \neq m_{H_d}^2 \neq m_0^2(M_{\text{GUT}}) \quad (3.34)$$

and uses the weak scale parameters  $\mu$  and  $m_A$  to replace the  $m_{H_u}^2$  and  $m_{H_d}^2$ .

$$\mu^2 = \frac{m_{H_d}^2 - m_{H_u}^2 \tan^2 \beta}{\tan^2 \beta - 1} - \frac{m_Z^2}{2} \quad (3.35)$$

$$m_A^2 = m_{H_d}^2 + m_{H_u}^2 + 2\mu^2 \quad (3.36)$$

If the value of NUHM2 free parameters are chosen as the following ranges

- $m_0 \sim 1$  to 7 TeV,
- $m_{1/2} \sim 0.3$  to 1.5 TeV,
- $A_0 \sim \pm(1 \text{ to } 2)m_0$ ,
- $\tan \beta \sim 5$  to 50,
- $\mu \sim 100$  to 300 GeV,
- $m_A \sim 1$  GeV

then the low EWFT can be achieved whilst keep all the SUSY spectrum and maintain  $123 < m_H < 127$  GeV. Comparing with the well-known mSUGRA/CMSSM models which have the lowest  $\Delta_{EW} \sim 200$ , the  $\Delta_{EW}$  in the NUHM2 model is about 10 only.

# Chapter 4

## The ATLAS Experiment at LHC

The European Organisation for Nuclear Research (CERN<sup>1</sup>) was founded in 1954 and is based in the suburb of Geneva on the Franco–Swiss border. The main function of CERN is to provide particle accelerators and detectors for high-energy physics research. The physicists and engineers at CERN are probing the fundamental structure of the universe using the world’s largest and most complex scientific facility — the *Large Hadron Collider* (LHC) [65]. In the LHC, the particles are boosted to high energies and collide at close to the speed of light. The results of the collisions are recorded by the various detectors. There are seven experiments at the LHC. The biggest of these experiments are *ATLAS* (A Toroidal LHC ApparatuS) [66] and *CMS* (Compact Muon Solenoid) [67] which use general-purpose detectors to investigate a broad physics programme ranging from the search for the Higgs boson to extra dimensions and particles that could make up dark matter. The *ALICE* (A Large Ion Collider Experiment) [68] experiment is designed to study the physics of quark-gluon plasma form and the *LHCb* (Large Hadron Collider beauty) [69] experiment specialises in investigating of CP violation<sup>2</sup> by studying the

---

<sup>1</sup>The name CERN is derived from the acronym for the French Conseil Européen pour la Recherche Nucléaire.

<sup>2</sup>The CP violation is violation of the charge conjugate and parity symmetry which says if a particle is interchanged with its anti-particle and its spatial coordinates are inverted, then the physics laws should be the same.

$b$ -quark. These four detectors sit underground in huge caverns of the LHC ring. The rest three experiments, *TOTEM* [70], *LHCf* [71], and *MoEDAL* [72], are smaller. The TOTEM (TOTal Elastic and diffractive cross section Measurement) [70] experiment aims at the measurement of total cross section, elastic scattering, and diffractive dissociation. The LHCf (Large Hadron Collider forward) [71] experiment is intended to measure the neutral particle produced by the collider using the forward particles. The prime motivation of the MoEDAL (Monopole and Exotics Detector at the LHC) [72] experiment is to search directly for the magnetic monopole. An overview of the LHC is described in Section 4.1 and the detector apparatus of the ATLAS experiment is outlined in Section 4.2.

## 4.1 The Large Hadron Collide

The LHC [65] is the world’s largest and most powerful accelerator which accelerates and collides protons in a 26.7 km circumference crossing the Franco–Swiss border 100 m underground. Built in the tunnel of the former *LEP* (Large Electron–Positron), the LHC is capable of colliding protons as well as heavy ions. Comparing with the LEP which collides electrons and positrons, the advantage of the LHC is the lower energy loss<sup>3</sup> in the synchrotron radiation, such that higher energies can be reached by the LHC. The LHC is designed for collisions at a centre-of-mass energy  $\sqrt{s} = 14$  TeV and an instantaneous luminosity of  $\mathcal{L} = 10^{34} \text{ cm}^{-2}\text{s}^{-1}$ . Figure 4.1 shows the infrastructure of the LHC and the pre-accelerator system.

The protons are extracted by ionisation from a hydrogen source and are accelerated to 50 MeV by the linear accelerator *LINAC2*. Then they are injected into the *Proton Synchrotron Booster* (PSB) where the proton energies are increased to 1.4 GeV before they

---

<sup>3</sup>The energy loss for protons is about eleven orders of magnitude smaller than the electrons.

## CERN's Accelerator Complex

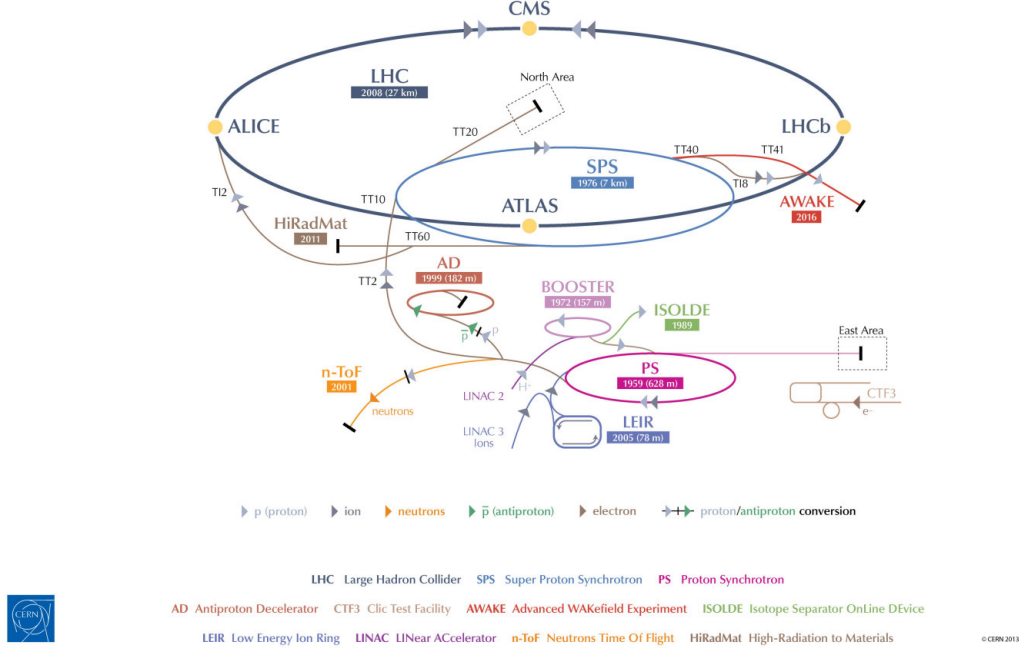


**Figure 4.1:** The accelerator complex at CERN [73].

enter the *Proton Synchrotron* (PS) which accelerates the protons to 25 GeV. Next, the proton energies are increasing to 450 GeV in the *Super Proton Synchrotron* (SPS). Finally, the protons are split into two beams and enter the LHC where the two beams run in two adjacent beam pipes with opposite directions. In order to keep the protons on the circular trajectory in the LHC, 1232 superconducting dipole magnets [74] generate a magnetic field strength of 8.33 T to bend the proton beams in eight arcs. Additionally, 392 quadrupole magnets [74] are installed to focus the beam. A cryogenic system running with super-fluid helium-4 is used to cool down the superconducting magnets to a temperature of 1.7 K.

For a given physics process, the event rate is proportional to the cross section  $\sigma$  of this process

$$\frac{dN}{dt} = \mathcal{L} \cdot \sigma \quad (4.1)$$

where  $N$  is the number of events and  $\mathcal{L}$  denotes the luminosity of the beam. The luminosity

of the beam,  $\mathcal{L}$ , can be calculated by

$$\mathcal{L} = \frac{N^2 f}{4\pi\sigma_x\sigma_y} \cdot F \quad (4.2)$$

where  $N$  is the number of protons,  $f$  is the bunches crossing frequency, and the  $\sigma_x$  and  $\sigma_y$  are the  $x$  and  $y$  components for cross section  $\sigma$ . The geometric luminosity reduction factor,  $F$ , is related to the crossing angle at the *interaction point* (IP). Considering a beam consisting of  $1.15 \times 10^{11}$  protons with bunching spacing of 25 ns, the transversal size of the bunch at IP  $16 \times 10^{-4}$  cm, and taking the geometric luminosity reduction factor as 1, the design luminosity of  $10^{34} \text{ cm}^{-2}\text{s}^{-1}$  can be reached.

The first beam was circulated through the collider on the morning of 10 September 2008 [75]. However, a magnet quench incident occurred on 19 September 2008 and caused extensive damage to over 50 superconducting magnets, their mountings, and the vacuum pipe. Most of 2009 was spent on repairs the damage caused by the magnet quench incident and the operations resumed on 20 November of that year. The first phase of data-taking (Run 1) started at the end of 2009 and the beam energy was increased to a centre-of-mass  $\sqrt{s} = 7$  TeV in 2011 and  $\sqrt{s} = 8$  TeV in 2012. The total integrated luminosity of  $5.46 \text{ fb}^{-1}$  was collected in 2011 and of  $22.8 \text{ fb}^{-1}$  was collected in 2012. Since 13 February 2013 the LHC was in the Long Shutdown 1 (LS1) phase for maintenance and upgrades. On 5 April 2015, the LHC restarted and was operating at a centre-of-mass energy  $\sqrt{s} = 13$  TeV throughout the Run 2 phase<sup>4</sup>.

---

<sup>4</sup>The Run 2 data-taking started from 2015.

## 4.2 The ATLAS experiment

The ATLAS<sup>5</sup> detector [66] is a multi-purpose detector housed in its cavern at point 1 at the LHC [65]. It is the largest experiment at the LHC with a length of 44 m, a diameter of 25 m, and a weight of approximately 7000 tonnes. It consists of three high precision sub-detector systems which are arranged concentrically around the interaction point and in forward and backward symmetrically. Related to this symmetry, the ATLAS detector is sectioned into the central barrel region with one end-cap region perpendicular to the beam pipe on either side. Figure 4.2 shows an overview of the ATLAS detector with its major components.

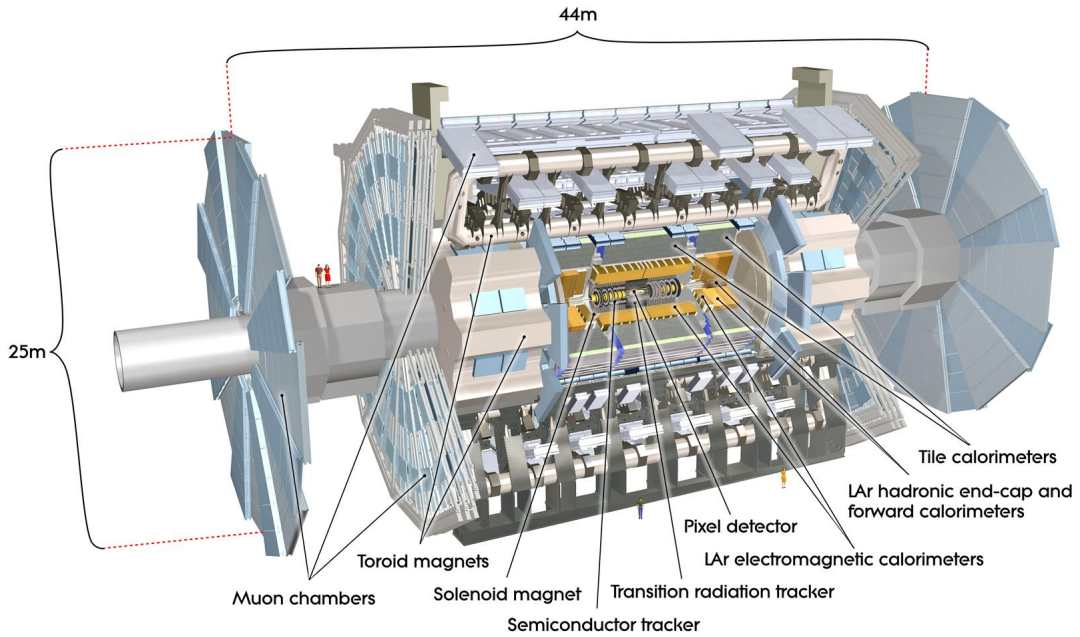


**Figure 4.2:** Overview of the ATLAS detector [66].

The ATLAS detector is designed to record the proton-proton interactions delivered by the LHC. It can identify particles and measure their tracks and energies with very high precision, therefore, it is sensitive to large areas of particle physics phenomena

---

<sup>5</sup>A Toroidal LHC Apparatus



from the precision measurement of the Standard Model to beyond the Standard Model (BSM). The detector is constituted by three sub-detector systems and the magnet system. The innermost part of the detector is called the *inner detector* which identifies and reconstructs the charged particles as well as the primary and secondary vertices. Around it, the *calorimeter* system is built as a cylindrical barrel with caps at each end to measure the particle energies. The detector is completed by the *muon spectrometer* which performs identification and measurement of momenta of muons. The magnetic system produces a field of  $B = 0.5$  T and  $B = 1$  T at barrel and two end-cap, respectively. The detector has to withstand large collision rates with approximately 1000 particles per collision, therefore, a fast readout and a three-level trigger system are implemented to reduce the event rate from 40 MHz to 200 Hz. The ATLAS coordinate system and the detail of each sub-detector systems are described in the following sections.

### 4.2.1 The ATLAS coordinate system

ATLAS uses a *right-handed coordinate system* with its origin at the nominal proton-proton interaction point (IP) in the centre of the detector and the  $z$ -axis along the beam pipe. Along the  $z$ -axis the detector is divided into side-A (positive  $z$ ) and side-C (negative  $z$ ). The positive  $x$ -axis is defined by the direction pointing from the interaction point to the centre of the LHC ring, and the positive  $y$ -axis points upward. The azimuthal angle  $\phi$  is measured around the beam pipe and the polar angle  $\theta$  is the angle from the  $z$ -axis. The transverse momentum  $p_T$ , the transverse energy  $E_T$  and the missing transverse energy  $E_T^{\text{miss}}$  are defined in the transverse plane<sup>6</sup>, here exemplary for  $p_T$

$$p_T = \sqrt{p_x^2 + p_y^2} \quad (4.3)$$

---

<sup>6</sup> $x - y$  plane

An important quantity in hadron collider physics is the *rapidity*,  $y$ , because of the invariance  $y$  under Lorentz boosts in the longitudinal direction. The rapidity is defined as

$$y = \frac{1}{2} \ln \left[ \frac{E + p_z}{E - p_z} \right] \quad (4.4)$$

where  $E$  denotes the particle energy and  $p_z$  is the component of the momentum along the beam direction. Since mainly leptons can be considered massless in respect to the nominal centre-of-mass energy, the pseudorapidity,  $\eta$ , is used instead of using the  $y$ . For a massless particle, the *pseudorapidity*,  $\eta$ , depends on the polar angle  $\theta$  through

$$\eta = -\ln \tan \frac{\theta}{2} \quad (4.5)$$

For a particle with the energy  $E$  much larger than its mass, the approximation  $E \approx |\vec{p}|$  is valid. The distance,  $\Delta R$ , between two objects in the  $\eta - \phi$  plan is given by

$$\Delta R = \sqrt{\Delta\eta^2 + \Delta\phi^2} \quad (4.6)$$

where  $\Delta\eta$  and  $\Delta\phi$  are the difference in pseudorapidity and azimuthal angle, respectively.

### 4.2.2 The inner detector and tracking system

The *inner detector* (ID) consists of three sub-detectors: the *pixel* detector, the *semiconductor tracker* (SCT), and the *transition radiation tracker* (TRT). The main purpose of the inner detector is to provide high precision measurements of the tracks of particles and to reconstruct the primary and secondary vertices. Each sub-detectors are composed of several layers of material which interacts with the charged particles when the charged particles penetrate the layers. A 2 T magnetic field generated by the central solenoid parallel to the beam axis is applied to bend the charged particles using the Lorentz force. By using the radius  $r$  of the curvature of the tracks, the magnetic field strength  $B$ , and

the charge of the particle  $q$ , we can calculate the magnitude of the transverse momentum

$p_T$

$$p_T = |q|Br \quad (4.7)$$

The layout of the inner detector is illustrated in Figure 4.3 and the detail of sub-detectors are described in the following paragraphs.

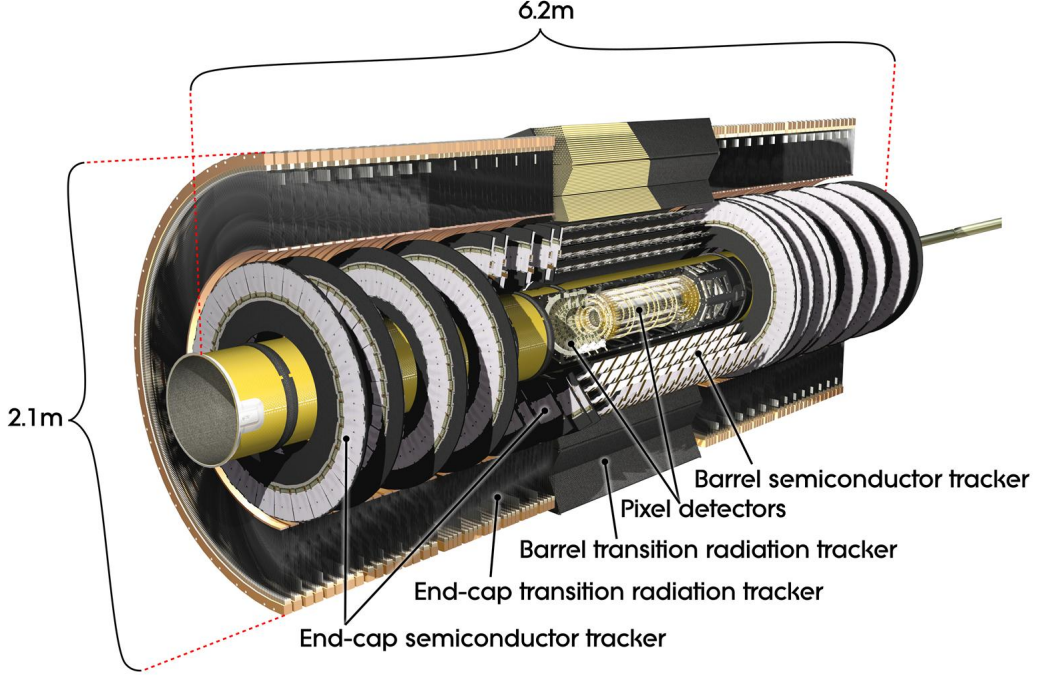


**Figure 4.3:** Cut-away view of the ATLAS inner detector [66].

### Pixel detector

The innermost part of the entire ATLAS detector components is the *pixel* detector which is composed of three barrel layers and three end-cap disks on each side. The three cylindrical barrel layers around the beam axis have radial positions of 50.5 mm, 88.5 mm, and 122.5 mm respectively and they are made of 22, 38, and 52 identical staves respectively. Each staff is inclined with azimuthal angle of 20 degrees and is composed of 13 pixel modules with 46,080 readout channel per module. The size of each pixel is  $50 \times 400 \mu m^2$

in  $R - \phi \times z$ . In the forward region, three disks on each side equip the modules identical to the barrel modules, except the connecting cables. The total 1,744 modules in the pixel detector lead to nearly 80 million channel readout and provide the intrinsic accuracy of  $10 \mu m$  in  $R - \phi$  plane and  $115 \mu m$  in  $z$  direction covering the region  $|\eta| < 2.5$ .

### **Semi conductor tracker**

On the top of the pixel detector is the *semi conductor tracker* (SCT) which is a silicon strip detector. There are about 6.3 million readout channels which are arranged in 4088 microstrips. The intrinsic accuracies per sensor is  $17 \mu m$  in  $R - \phi$  and  $580 \mu m$  in  $z$  direction for the barrel and in  $R$  for the disks, respectively. Similar to the pixel detector, the SCT covers the region  $|\eta| < 2.5$  and consists of 8 strip layers in barrel and a total of 9 discs in the end-cap region on each side. No track reconstruction is possible beyond the covered pseudorapidity range. Therefore, the electrons cannot be distinguished from photons above  $|\eta| > 2.5$  region.

### **Transition radiation tracker**

The outermost component of the inner detector is the *transition radiation tracker* (TRT) which consists of 4 mm diameter straw tubes filled with the xenon-based gas mixture. The gas mixture are ionised by charged particles when they penetrates the straws. The ionised electrons drift to the cathode because a high voltage is applied on the tungsten wire in the center of the straw tube. Therefore, the TRT allows the enhanced electron identification, momentum measurement, vertex measurement. In the barrel region, the straws are surrounded by polypropylene fibres and are divided into two halves at  $|\eta| = 0$ . In the end-caps, the straws are arranged radially and surrounded by foils as a transition radiation element. They are read out at two sides and at the center of the TRT with the

total number of the readout channels of TRT are approximately 350,000. The TRT only provides information in the  $R - \phi$  plane with an intrinsic accuracy of  $130 \mu\text{m}$  per straw and covers a range up to  $|\eta| < 2.0$ .

### Solenoid magnet

A superconducting solenoid magnet encloses the inner detector and produces a 2 T magnetic field to bend the trajectories of the charged particles. A cooling system is used and shared with the *electromagnetic calorimeter* (Section 4.2.3) to reduced the deterioration of the energy measurement.

### 4.2.3 The calorimeters

The calorimeters are used to measure the energy of particles, such as electrons, photons, and jets. Besides muons and neutrinos, all other particles interacting electromagnetically or hadronically are stopped in the calorimeters by absorbing their energy. Not only charged particles but also neutral particles such as photons and neutral hadrons can be detected in the calorimeters. By requiring highly hermiticity of the calorimeters, the missing energy  $E_{\text{T}}^{\text{miss}}$  can be reconstructed precisely as negative vectorial sum of all energy deposits. The ATLAS calorimeter system is placed between the inner detector (Section 4.2.2) and the muon spectrometer (Section 4.2.4). The ATLAS calorimeter system consists of an inner *electromagnetic calorimeter* and an outer *hadronic calorimeter* together with the *forward calorimeter*. The electromagnetic calorimeter and hadronic calorimeter are *sampling calorimeters* which consist of two different materials alternately.

An absorber material is used to enhance the particle showers<sup>7</sup> and a highly ionisable active

---

<sup>7</sup>The shower is the cascade of secondary particles produced by the high-energy particle interacting with dense material.

medium is used to measure the deposited energy. Because only the energies deposited in the active medium can be observed, the total energy of the shower can be estimated from the deposited energy by clustering algorithms. The electromagnetic calorimeter is focusing on measuring electrons and photons, and the hadronic calorimeter is dedicated for hadronically interacting particles. The whole ATLAS calorimeter system covers a range  $|\eta| < 4.9$ . An layout view of the ATLAS calorimeter system is shown in Figure 4.4 and the detail of the three calorimeters are described in the following paragraphs.

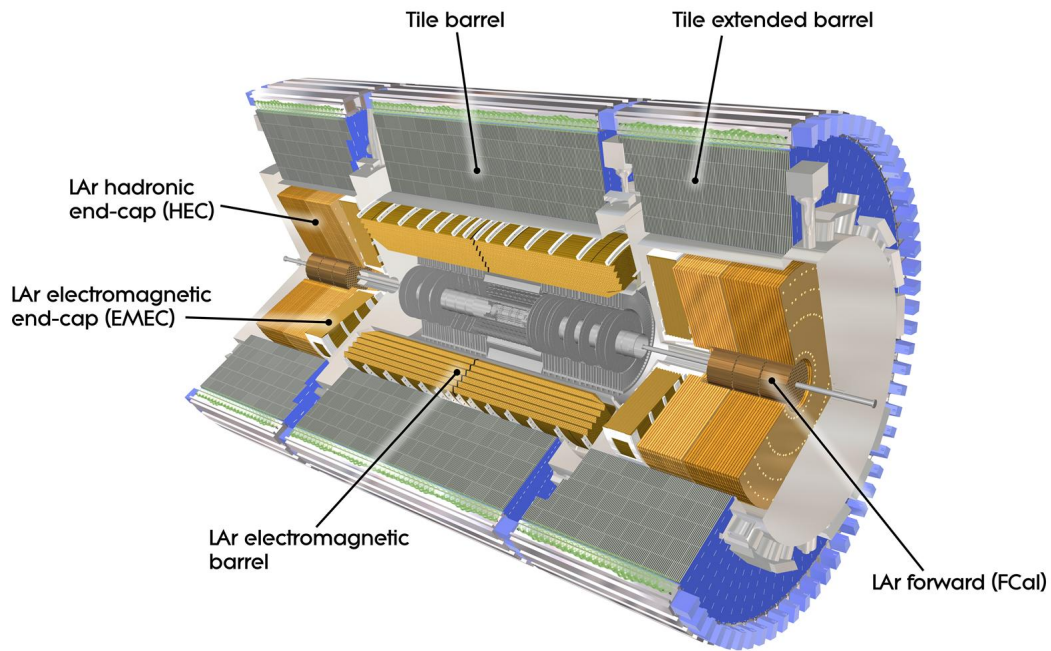


**Figure 4.4:** Cut-away view of the calorimeter system [66].

## Electromagnetic calorimeter

The *electromagnetic calorimeter* (ECAL) measures the energy of electrons and photons as they interact with matter. The ECAL consists of accordion shaped cells of alternating layers of lead as absorber material and liquid argon (LAr) as active medium. The accordion shaped provides the full coverage in the azimuthal angle  $\phi$ . The LAr is chosen as an active

medium because it is hard to radiate, it has stable response time and linear behaviour [66]. The electrons or photons lose their energies by alternating bremsstrahlung and pair production when they interact with lead and result in the electromagnetic particle showers which ionise the LAr and the ionisation currents are collected by the copper electrodes. The ECAL is divided into barrel (EMB) and end-cap (EMEC) components, which cover  $|\eta| < 1.475$  and  $1.375 < |\eta| < 3.2$ <sup>8</sup>, respectively. The EMB is made up of three longitudinal layers with different granularity and sensitive in the region  $|\eta| < 2.5$ . The first strip layer has the highest granularity where the size of cells corresponding to  $\Delta\eta \times \Delta\phi = 0.0031 \times 0.1$  for  $|\eta| < 1.8$  and coarser for larger  $|\eta|$ . The smallest granularity allows to separate the showers coming from electrons, photons and neutral pions. The second layer is the largest part of the EMB with the size of cells corresponding to  $\Delta\eta \times \Delta\phi = 0.025 \times 0.0245$  so most of the energies are deposited in this layer. The third layer has the granularity  $\Delta\eta \times \Delta\phi = 0.05 \times 0.0245$ . The total thickness are  $22 X_0$ <sup>9</sup> and  $24 X_0$  for EMB and EMECs, respectively. This special thickness is sufficient to prevent the punch-throughs of high energy showers into the muon spectrometer. Figure 4.5 shows the cut-away view of the the accordion shaped EMB module with the dimensions for three layers.

## Hadronic calorimeter

The electromagnetic interacting particles produce narrow showers, however, the hadrons, which are heavier and penetrate medium further, produce more wide-spread hadronic showers. The *hadronic calorimeter* (HCAL) surrounds the ECAL and is made up by a barrel and two end-caps (HEC). The barrel covers  $|\eta| < 1.7$  and it uses plastic scintillator tiles as active medium and steel as absorber material. The hadronic showers stimulate

---

<sup>8</sup>There are two EMECs and each of them consists of two wheels. The inner wheel covers  $1.375 < |\eta| < 2.5$  and the outer wheel covers  $2.5 < |\eta| < 3.2$ .

<sup>9</sup>The  $X_0$  stands for radiation lengths which is a characteristic of material. It is related to the energy loss of the particle when it interacts with the material electromagnetically.

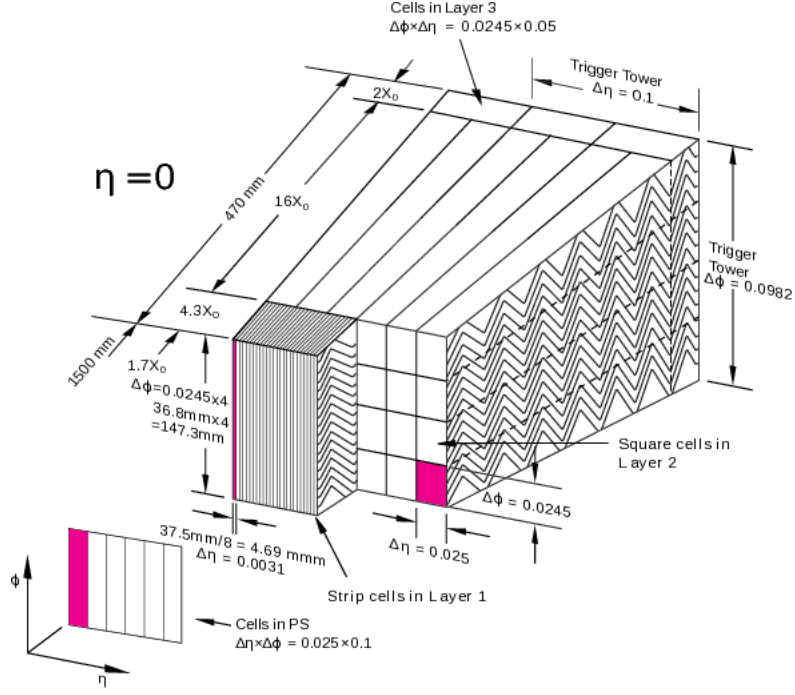


**Figure 4.5:** Cut-away view of the accordion shaped EMB module with the dimensions for three layers [76].

the scintillator and emit light which is collected by *photo multiplier tubes* (PMTs) and then read-out via wavelength shifting optical fibers. The HEC covers  $1.5 < |\eta| < 3.2$  which overlap with the pseudorapidity coverage region of barrel. The HEC is composed of two copper plate wheels as absorber material on each side and the LAr in between. The designed thickness in the barrel region is  $9.7 \lambda$ <sup>10</sup>. Therefore, the punch-through to the muon spectrometer is suppressed. The granularity of the HCAL is coarser than the ECAL but it is sufficient for measuring  $E_T^{\text{miss}}$  and jet reconstruction.

### Forward calorimeter

The *forward calorimeter* (FCAL) uses the LAr as active medium and one copper and two tungsten layers as absorber materials. The copper layer (FCAL1) is used to measure

<sup>10</sup>The  $\lambda$  represents the hadronic interaction lengths which is the mean free path of a strongly interacting particle between two inelastic scatterings.



the electromagnetic interactions whereas the two tungsten layers (FCAL2 and FCAL3) is used to measure the hadronically interactions. The FCAL provides the very forward region coverage  $3.1 < |\eta| < 4.9$  can contribute the  $E_T^{\text{miss}}$  measurement.

## Energy resolution

The energy resolution is the ability of the calorimeter to distinguish the two adjacent energies. The number of ionized particles  $N$  is proportion to the energy  $E$  of the incoming particle. Therefore, the higher energy of the incoming particle the more ionised particles produced in the shower. Based on the Poisson statistics we know

$$\frac{\sigma_E}{E} \propto \frac{\sigma_N}{N} = \frac{\sqrt{N}}{N} = \frac{1}{\sqrt{N}} \propto \frac{1}{\sqrt{E}} \quad (4.8)$$

where  $\sigma_E$  is the energy resolution at FWHM<sup>11</sup> in a Gaussian distribution and  $\sigma_N = \sqrt{N}$  is the Poisson standard deviation. Taking the effects of calibration and electronics noise into account, the relative energy resolution becomes

$$\frac{\sigma_E}{E} = \frac{a}{E} \oplus \frac{b}{\sqrt{E}} \oplus c \quad (4.9)$$

where  $a, b, c$  are noise, sampling, and constant terms, respectively. The relative energy resolutions for ECAL, HCAL, and FCAL are summarised in Table 4.1.

Calorimeter	Required resolution
Electromagnetic calorimeter	$\sigma_E/E = 10\%/\sqrt{E(\text{GeV})} \oplus 0.7\%$
Hadronic calorimeter	$\sigma_E/E = 50\%/\sqrt{E(\text{GeV})} \oplus 3\%$
Forward calorimeter	$\sigma_E/E = 100\%/\sqrt{E(\text{GeV})} \oplus 10\%$

**Table 4.1:** Resolution requirements for the different calorimeters of the ATLAS detector [66].

<sup>11</sup>The FWHM means full width at half maximum.

#### 4.2.4 The muon spectrometer

The outermost part of the ATLAS detector is the *muon spectrometer* [66, 77, 78]. Muons have the same properties as electrons but 200 times heavier than the electrons. Because muons don't interact predominately by bremsstrahlung, most of the muons escape the inner detector and calorimeters without being stopped. Only the muons with an energy less than 5 GeV are stopped before the muon spectrometer. Therefore, a detector concentrates on the measurement of high precision momentum and trajectory of muons is necessary.

The muon spectrometer is designed to measure the transverse momentum ( $p_T$ ) of muons with  $p_T > 3$  GeV with a resolution of 3% for  $p_T < 250$  GeV and increasing to 10% at 1 TeV. It consists of large toroid magnets system and high precision tracking chambers allowing a precise measurement of the muon momentum over nearly the full solid angle. The barrel toroid magnet system is composed of eight superconducting coils which are installed radial symmetrically around the beam pipe. It covers the range  $|\eta| < 1.4$  and bends the trajectories of muons with the bending power 1.5 to 5.5 Tm. The magnetic field produced by the barrel toroid magnets provides an approximately 1 T field at the center of each coils, but is rather non-uniform, especially in the barrel-endcap transition region. In the endcap toroid magnets system, the magnetic field is provided by eight superconducting coils, closed in an insulation vessel extending to about 10 m in diameter, located between the first and the second station of tracking chambers. The endcap toroid magnets cover  $1.6 < |\eta| < 2.4$  and provide a magnetic field in the range of 1 to 2 T with bending power 1 to 7.5 Tm.

The *monitored drift tubes* (MDT) consists of cylindrical drift tubes, filled with a gas mixture of Ar and CO<sub>2</sub>. A tungsten-rhenium alloyed aluminium wire in the centre of each tube collects the electrons freed by ionisation of the gas volume by traversing muons. The

MDT covers a full range of  $|\eta| < 2.7$ , while the inner layer only covers  $|\eta| < 2.0$ . The *cathode strip chambers* (CSC) provides a coverage range  $2.0 < |\eta| < 2.7$ , where MDTs would have occupancy problems. The CSC is made up by two discs and filled with Ar and CO<sub>2</sub> gas mixture. Both MDT and CSC are slow for trigger but they provide high precision tracking in the spectrometer bending plane and end-cap inner layer, respectively. The *resistive plate chambers* (RPC) and *thin gap chambers* (TGC) are used for triggering in barrel and end-cap, they have sufficient intrinsic time resolution of 1.5 ns and 4 ns, respectively. A sketch of the muon spectrometer and its four components are depicted in Figure 4.6 and Table 4.2 gives a summary of the muon spectrometer components.

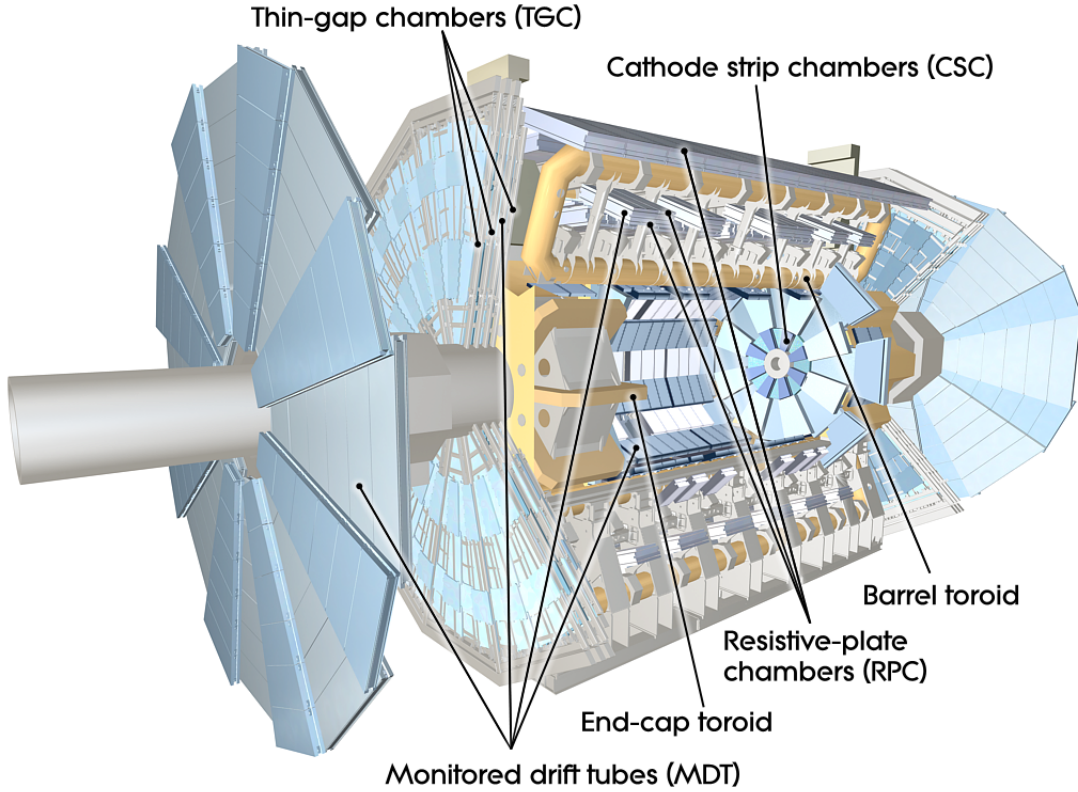


**Figure 4.6:** Sketch of the muon system of the ATLAS detector [66].

Type	Purpose	Location	$\eta$ coverage	Channel
MDT	Tracking	barrel + end-cap	$0.0 < \eta < 2.7$	354k
CSC	Tracking	end-cap layer 1	$2.0 < \eta < 2.7$	30.7k
RPC	Trigger	barrel	$0.0 < \eta < 1.0$	373k
TGC	Trigger	end-cap	$1.0 < \eta < 2.4$	318k

**Table 4.2:** A summary of the muon spectrometer components.

### 4.2.5 The trigger system and data acquisition

The LHC  $pp$  collision rate is 40 MHz corresponding to 50 TB/s data<sup>12</sup> generated by the ATLAS detector [79]. However, the limited rate for writing the events into disk is about 1 kHz<sup>13</sup>. The majority of the products of the  $pp$  collision are low  $p_T$  QCD processes which are not the interesting events for the analysis. Hence, the three-level ATLAS trigger and data acquisition (DAQ) system is designed to pick the interesting events and reduce the data size. Figure 4.7 shows the functional view of the ATLAS trigger/DAQ system and the brief descriptions are given in the following paragraph.

#### The level-1 trigger

The initial selection is made by the hardware-based *level-1* (LVL1) trigger based on reduced-granularity information from calorimeters and the muon spectrometer. The latency<sup>14</sup> of the level-1 trigger is required to be less than  $2.5 \mu s$ <sup>15</sup>. The high  $p_T$  muons are identified using only RPC and TGC. The high  $p_T$   $e/\gamma$ , jets, hadronically decaying  $\tau$ -leptons, large  $E_T^{\text{miss}}$  and total  $E_T$  objects are selected by calorimeter trigger using a

<sup>12</sup>Assuming the typical event size is 1.3 MB.

<sup>13</sup>The data storage rate is 200 Hz in Run-1 but it is increased to about 1 kHz in Run-2.

<sup>14</sup>The latency is the time interval from the  $pp$  collision until trigger decision is available to the front-end electronics.

<sup>15</sup>The target latency for the level-1 trigger is  $2.0 \mu s$ .

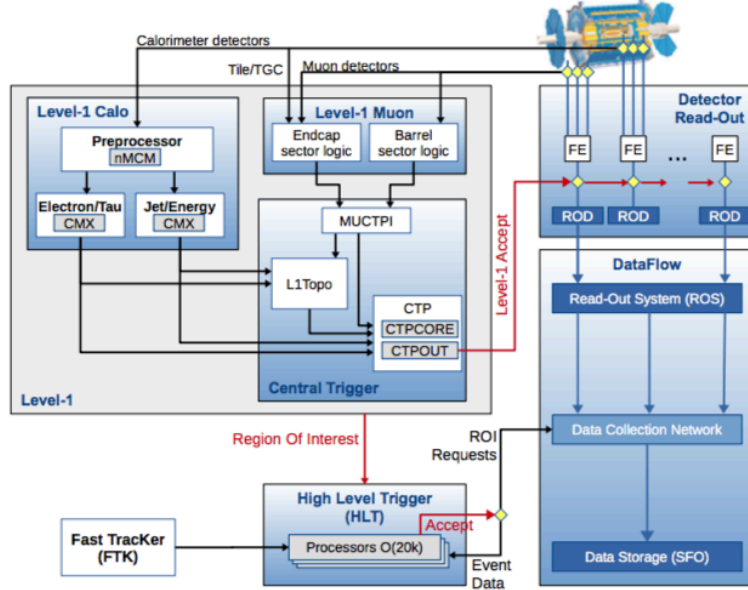


**Figure 4.7:** The schematic view of the ATLAS trigger/DAQ system in Run-2. The figure is taken from [80].

number of sets of  $p_T$  thresholds<sup>16</sup> and the energy isolation cuts can be applied. The selected events are read out from the front-end electronics into *readout drivers* (RODs) and written into *readout buffers* (ROBs). The information such as the  $p_T$ ,  $\eta$ , and  $\phi$  of the candidate objects and  $E_T^{\text{miss}}$  and total  $E_T$  are saved into *region-of-interest* (ROI) and send to the high level trigger. The level-1 trigger reduces the event rate from the high LHC bunch crossing rate to 100 kHz.

### The high level trigger

The *level-2* trigger and *event filter* (EF) computer clusters used in Run-1 are merged into a single event processing *high level trigger* (HLT) farm in Run-2. This combination reduces the complexity, allows resource sharing between algorithms, and results in a more flexible HLT. The HLT is completely software based trigger system and it uses the ROI

<sup>16</sup>Typically, there are 6 to 8 sets of thresholds per object type.

information from the level-1 trigger and the tracking information from the inner detector. The full-event track reconstruction information is performed by the *fast tracker* (FTK) system after each level-1 trigger and provided to the HLT. The trigger reconstruction algorithms for HLT were re-optimised to minimise the differences between the HLT and the offline analysis selections. The output rate of the HLT is approximately 1 kHz within a processing time about  $200\ \mu s$ .

# Chapter 5

## Data set and simulated events

This chapter describes the collision data and simulated event samples used in searching for electroweak production of SUSY states in the compressed scenarios. The collision data are presented in Sect. 5.1 and the Monte Carlo (MC) simulated event samples are detailed in Sect. 5.2. The samples used for searching the strongly-produced SUSY particles in final states with two same-sign or three lepton and jets (SS/3L+jets) can be found in the App. A.1.

### 5.1 Collision data

The  $pp$  collision data used in this analysis were collected by the ATLAS detector at  $\sqrt{s} = 13$  TeV during 2015 and 2016 at LHC. The data corresponds to an integrated luminosity of  $36.1 \text{ fb}^{-1}$  ( $3.2 \text{ fb}^{-1}$  in 2015 and  $32.9 \text{ fb}^{-1}$  in 2016) with a combined uncertainty of 2.1% after applying beam, detector, and data-quality requirements. The combined uncertainty is derived following the methodology similar to those described in Ref. [81]. The average number of  $pp$  interactions per bunch crossing (pile-up) is 13.5 in the 2015 data set and is 25 in the 2016 data set. The data samples are required to satisfy the following good runs list (GRLs) as recommended by the ATLAS collaboration

- `data15_13TeV.periodAllYear_DetStatus-v79-repro20-02.DQDefects-00-02-02_PHYS.StandardGRL_All_Good_25ns.xml`
- `data16_13TeV.periodAllYear_DetStatus-v88-pro20-21.DQDefects-00-02-04_PHYS.StandardGRL_All_Good_25ns.xml`

Events are selected using different inclusive  $E_T^{\text{miss}}$  triggers depending on the run period as listed in Table. 5.1. Two new triggers, `HLT_mu4_j125_xe90_mht` and `HLT_2mu4_j85_xe50_mht`, are developed for compressed scenarios starting from run number 308084. However, these new triggers only contribute a small gain compared to the inclusive  $E_T^{\text{miss}}$  triggers. This analysis uses inclusive  $E_T^{\text{miss}}$  triggers only.

Run period	$E_T^{\text{miss}}$ trigger
2015	<code>HLT_xe70_mht</code>
A-D3	<code>HLT_xe90_mht_L1XE50</code>
D4-F1	<code>HLT_xe100_mht_L1XE50</code>
F1-	<code>HLT_xe110_mht_L1XE50</code>

**Table 5.1:** The inclusive  $E_T^{\text{miss}}$  triggers used in this analysis. The  $E_T^{\text{miss}}$  threshold varies from 70 to 110 GeV depending on the run period.

## 5.2 Monte Carlo simulated event samples

MC samples are used to model the SUSY signals and to estimated the SM background. All SM background MC samples were processed through a detailed ATLAS detector simulation based on GEANT4 [82] and the SUSY signal samples were simulated by a fast simulation (AF2) that parameterizes the calorimeter response [83]. To simulate the effects of additional  $pp$  collisions (pile-up) in the same and nearby bunch crossings, inelastic interactions were generated using the soft QCD processes of PYTHIA v8.186 [84] with A2 tune [85] and the MSTW2008LO PDF set [86]. These MC events were overlaid onto each



simulated hard-scatter event and reweighted to match the pile-up conditions observed in the data.

### 5.2.1 The SM background samples

The SHERPA 2.1.1, 2.2.1, and 2.2.2 [87] were used to produce the  $Z^{(*)}/\gamma^* + \text{jets}$ , diboson, and triboson events. The matrix elements (ME) were calculated for up to two partons at next-to-leading order (NLO) and up to four partons at leading order (LO) depending on the process. The  $Z^{(*)}/\gamma^* + \text{jets}$  and diboson samples cover the dilepton invariant masses from 0.5 GeV for  $Z^{(*)}/\gamma^* \rightarrow e^+e^-/\mu^+\mu^-$  and from 3.8 GeV for  $Z^{(*)}/\gamma^* \rightarrow \tau^+\tau^-$ . The POWHEG-Box v1 and v2 interfaced to PYTHIA 6.428 were used to simulated  $t\bar{t}$  and single-top production at NLO in the ME. The Higgs boson production were generated using POWHEG-Box v2 interfaced to PYTHIA 8.186. A Higgs boson in association with a  $W$  or  $Z$  boson production was simulated using MG5\_AMC@NLO 2.2.2 with PYTHIA 8.186 and the ATLAS A14 tune. The processes containing  $t\bar{t}$  and at least one electroweak bosons were produced using MG5\_AMC@NLO 2.2.1, 2.2.2, 2.3.2, 2.3.3 with PYTHIA 6.4.28 or 8.186. These processes were generated at NLO in the ME except for  $t + Z$  and  $t + t\bar{t}$  which were produced at LO. Table 5.2 summarizes the event generator configurations of the ME, parton shower, PDF set, and the cross-section normalization. Except those produced by SHERPA event generator, the EVTGEN v1.2.0 [88] was used to model the decay of bottom and charm hadrons in all MC samples.

### 5.2.2 The SUSY signal samples

The NUHM2 model allows the masses of the Higgs doublets  $m_{H_u}$  and  $m_{H_d}$  differ from the universal scalar mass  $m_0$  at the GUT scale. The parameters of the NUHM2 model were

Process	Matrix element	Parton shower	PDF set	Cross-section
$Z^{(*)}/\gamma^* + \text{jets}$	SHERPA 2.2.1		NNPDF 3.0 NNLO	NNLO
Diboson	SHERPA 2.1.1 / 2.2.1 / 2.2.2		NNPDF 3.0 NNLO	Generator NLO
Triboson	SHERPA 2.2.1		NNPDF 3.0 NNLO	Generator LO, NLO
$t\bar{t}$	POWHEG-Box v2	PYTHIA 6.428	NLO CT10	NNLO + NNLL
$t$ ( $s$ -channel)	POWHEG-Box v1	PYTHIA 6.428	NLO CT10	NNLO + NNLL
$t$ ( $t$ -channel)	POWHEG-Box v1	PYTHIA 6.428	NLO CT10f4	NNLO + NNLL
$t + W$	POWHEG-Box v1	PYTHIA 6.428	NLO CT10	NNLO + NNLL
$h(\rightarrow \ell\ell, WW)$	POWHEG-Box v2	PYTHIA 8.186	NLO CTEQ6L1	NLO
$h + W/Z$	MG5_AMC@NLO 2.2.2	PYTHIA 8.186	NNPDF 2.3 LO	NLO
$t\bar{t} + W/Z/\gamma^*$	MG5_AMC@NLO 2.3.3	PYTHIA 8.186	NNPDF 3.0 LO	NLO
$t\bar{t} + WW/t\bar{t}$	MG5_AMC@NLO 2.2.2	PYTHIA 8.186	NNPDF 2.3 LO	NLO
$t + Z$	MG5_AMC@NLO 2.2.1	PYTHIA 6.428	NNPDF 2.3 LO	LO
$t + WZ$	MG5_AMC@NLO 2.3.2	PYTHIA 8.186	NNPDF 2.3 LO	NLO
$t + t\bar{t}$	MG5_AMC@NLO 2.2.2	PYTHIA 8.186	NNPDF 2.3 LO	LO

**Table 5.2:** The MC simulated samples of SM background process.

fixed to  $m_0 = 5$  TeV,  $m_A = 1$  TeV,  $A_0 = -1.6m_0$ ,  $\tan\beta = 15$ ,  $\mu = 150$  GeV, and the  $m_{1/2}$  is varied from 350 to 800 GeV as suggested in Ref. [57]. These parameter settings lead to RNS with low EWFT which keeps the Higgs boson mass about 125 GeV, the masses of  $\tilde{g}$  and  $\tilde{q}$  about TeV scale, and the light Higgsino mass about  $\mu$ . The mass spectra and decay branching ratios were calculated using ISAJET v7.84 [89] and the cross-sections were calculated to NLO in the strong coupling constant using PROSPINO v2.1 [90].

## The NUHM2 mass spectra

Figure 5.1 shows the mass spectra of the charginos  $\tilde{\chi}_{1,2}^\pm$  and neutralinos  $\tilde{\chi}_{1,2,3,4}^0$  as a function of  $m_{1/2}$  in the NUHM2 model and the mass splitting spectra between electroweakinos as a function of  $m_{1/2}$  are shown in Fig. 5.2. The masses of lower mass electroweakinos  $\tilde{\chi}_{1,2}^0$  and  $\tilde{\chi}_1^\pm$  are roughly flat when  $m_{1/2} > 500$  GeV, however, the masses of higher mass electroweakinos  $\tilde{\chi}_{3,4}^0$  and  $\tilde{\chi}_2^\pm$  increased with  $m_{1/2}$ . The mass differences between the lower

mass electroweakinos decrease with  $m_{1/2}$  and the mass splitting between  $\tilde{\chi}_3^0$  and the lower mass chargino  $\tilde{\chi}_1^\pm$  or neutralinos  $\tilde{\chi}_{1,2}^0$  increase with  $m_{1/2}$ . In the NUHM2 model, the  $m_{\tilde{\chi}_1^\pm}$  doesn't set to exactly in the middle between  $m_{\tilde{\chi}_1^0}$  and  $m_{\tilde{\chi}_2^0}$  but it varied such that the mass ratio varies from 1.61 to 1.21 as shown in Table 5.3.

**Figure 5.1:** The mass spectra of the charginos  $\tilde{\chi}_{1,2}^\pm$  and neutralinos  $\tilde{\chi}_{1,2,3,4}^0$  as a function of  $m_{1/2}$  in the NUHM2 model. The  $m_{\tilde{\chi}_1^0}$ ,  $m_{\tilde{\chi}_2^0}$ , and  $m_{\tilde{\chi}_1^\pm}$  are roughly flat when  $m_{1/2} > 500$  GeV. The  $m_{\tilde{\chi}_3^0}$ ,  $m_{\tilde{\chi}_4^0}$ , and  $m_{\tilde{\chi}_2^\pm}$  are heavier and increase with  $m_{1/2}$ .

**Figure 5.2:** The mass splitting spectra between charginos and neutralinos in the NUHM2 model. The mass differences between  $(\tilde{\chi}_3^0, \tilde{\chi}_{1,2}^0)$  and  $(\tilde{\chi}_3^0, \tilde{\chi}_1^\pm)$  increase with  $m_{1/2}$ . The mass differences between  $(\tilde{\chi}_1^\pm, \tilde{\chi}_1^0)$ ,  $(\tilde{\chi}_2^0, \tilde{\chi}_1^0)$ , and  $(\tilde{\chi}_2^0, \tilde{\chi}_1^\pm)$  decrease with  $m_{1/2}$ .

$m_{1/2}$ [GeV]	$m_{\tilde{\chi}_2^0}$ [GeV]	$m_{\tilde{\chi}_1^\pm}$ [GeV]	$m_{\tilde{\chi}_1^0}$ [GeV]	$(m_{\tilde{\chi}_2^0} - m_{\tilde{\chi}_1^\pm}) / (m_{\tilde{\chi}_1^\pm} - m_{\tilde{\chi}_1^0})$
350	161.68	144.29	115.62	1.61
400	161.14	147.54	122.97	1.55
500	160.30	151.47	132.28	1.46
600	159.66	153.71	137.61	1.37
700	159.17	155.14	140.98	1.28
800	158.78	156.14	143.29	1.21

**Table 5.3:** The masses of  $\tilde{\chi}_1^0$ ,  $\tilde{\chi}_2^0$ , and  $\tilde{\chi}_1^\pm$  and the ratios of the mass difference between  $(m_{\tilde{\chi}_2^0} - m_{\tilde{\chi}_1^\pm})$  and  $(m_{\tilde{\chi}_1^\pm} - m_{\tilde{\chi}_1^0})$ .

## The NUHM2 cross-sections

The electroweakinos are divided into two categories, compressed and accessible, in the NUHM2 model. The compressed category contains the lower mass charginos  $\tilde{\chi}_1^\pm$  and neutralinos  $\tilde{\chi}_{1,2}^0$  and the accessible category contains the higher mass charginos  $\tilde{\chi}_2^\pm$  and neutralinos  $\tilde{\chi}_{3,4}^0$ . Figure 5.3 shows the cross-sections for different combinations of electroweakino production and the detail values can be found in App. B. The largest cross-section is the compressed + compressed production and is almost independent of  $m_{1/2}$ . The cross-section of compressed + accessible and accessible + accessible productions are much smaller than the compressed + compressed production and they decrease quickly when  $m_{1/2}$  increases. Therefore, only the different combinations of compressed production are considered in this analysis. The compressed + compressed production has cross-section about  $pb$  scale at 13 TeV, hence the Higgsino analysis is expected to have good sensitivity for NUHM2 model.

**Figure 5.3:** The NUHM2 cross-sections. The cross-sections of individual combination are presented in dashed lines and the cross-sections for compressed + compressed, compressed + accessible, and accessible + accessible are represented in solid lines.

## The NUHM2 production channels and relevant decays

The compressed category contains  $\tilde{\chi}_1^\pm$ ,  $\tilde{\chi}_1^0$ , and  $\tilde{\chi}_2^0$ . Therefore, the compressed + compressed productions can be specified by  $\tilde{\chi}_1^0\tilde{\chi}_1^0$ ,  $\tilde{\chi}_1^0\tilde{\chi}_2^0$ ,  $\tilde{\chi}_1^0\tilde{\chi}_1^\pm$ ,  $\tilde{\chi}_2^0\tilde{\chi}_2^0$ ,  $\tilde{\chi}_2^0\tilde{\chi}_1^\pm$ , and  $\tilde{\chi}_1^\pm\tilde{\chi}_1^\mp$ . Because the highest sensitivity of this analysis is expected using 2 leptons, only the productions containing 2 leptons are considered. The  $R$ -parity conservation requires  $\tilde{\chi}_1^0$ , which is LSP, to be stable, therefore, the  $\tilde{\chi}_1^0\tilde{\chi}_1^0$  production doesn't pass 2 leptons requirement. The

cross-section of  $\tilde{\chi}_2^0\tilde{\chi}_2^0$  production is very low so it can be neglected. The  $\tilde{\chi}_1^\pm$  decays into a  $W^\pm$  and a  $\tilde{\chi}_1^0$ , therefore, the  $\tilde{\chi}_1^0\tilde{\chi}_1^\pm$  doesn't produce 2 leptons in the final state. Only the  $\tilde{\chi}_2^0\tilde{\chi}_1^0$ ,  $\tilde{\chi}_2^0\tilde{\chi}_1^\pm$ , and  $\tilde{\chi}_1^\pm\tilde{\chi}_1^\mp$  productions are considered in this analysis.

The neutralino  $\tilde{\chi}_2^0$  can decay into  $\gamma\tilde{\chi}_1^0$ ,  $W^\pm\tilde{\chi}_1^\mp$ ,  $q\bar{q}\tilde{\chi}_1^0$ ,  $\ell^+\ell^-\tilde{\chi}_1^0$ , and  $\nu\bar{\nu}\tilde{\chi}_1^0$ . Table 5.4 lists the branching ratios for all possible  $\tilde{\chi}_2^0$  decays for  $m_{1/2} = 600$  GeV. Since the  $\tilde{\chi}_2^0 \rightarrow \gamma\tilde{\chi}_1^0$  has very small branching ratio, this decay can be neglected.

The MC samples for the  $\tilde{\chi}_2^0\tilde{\chi}_1^\pm$  generated by  $pp$  collision are produced where four kinds of  $\tilde{\chi}_2^0$  decay are specified to determine the dominant one and the  $\tilde{\chi}_1^\pm$  decay is assumed to be  $\tilde{\chi}_1^\pm \rightarrow W^\pm\tilde{\chi}_1^0 \rightarrow f\bar{f}\tilde{\chi}_1^0$ . Since  $\tilde{\chi}_2^0 \rightarrow q\bar{q}\tilde{\chi}_1^0$  and  $\tilde{\chi}_2^0 \rightarrow \nu\bar{\nu}\tilde{\chi}_1^0$  do not satisfy the 2 leptons requirement, the  $\tilde{\chi}_2^0$  decay should be dominated by  $\tilde{\chi}_2^0 \rightarrow W^\pm\tilde{\chi}_1^\mp$  and  $\tilde{\chi}_2^0 \rightarrow \ell^+\ell^-\tilde{\chi}_1^0$ . Table 5.5 shows the 2 leptons filter efficiency for the  $\tilde{\chi}_2^0$  decays considered, the number of events in each decay type, and the percentage in the  $\tilde{\chi}_2^0$ . Because the  $\tilde{\chi}_2^0 \rightarrow \ell^+\ell^-\tilde{\chi}_1^0$  contributes more than 99%, the other 3 decays can be neglected. Although  $\tilde{\chi}_2^0 \rightarrow q\bar{q}\tilde{\chi}_1^0$  and  $\tilde{\chi}_2^0 \rightarrow \nu\bar{\nu}\tilde{\chi}_1^0$  are expected to contribute nothing, due to the presence of the fake leptons, there are some contributions. This is expected, as no requirement on the truth matching was used in the selection.

## The NUHM2 generation

The NUHM2 signal events were generated using MG5\_AMC@NLO v2.4.2 with NNPDF23LO PDF set up to two extra partons in the ME. The MADSPIN ?? were used to decay the electroweakinos which were required to produce at least two leptons in the final state. Then the results were interfaced with PYTHIA v8.186 using the A14 tune to model the parton shower (PS) and hadronization.

Decay	Branching Ratio	type
$\tilde{\chi}_2^0 \rightarrow \gamma \tilde{\chi}_1^0$	$3.91677720 \times 10^{-3}$	-
$\tilde{\chi}_2^0 \rightarrow \tilde{\chi}_1^- u \bar{d}$	$7.45565048 \times 10^{-4}$	$\tilde{\chi}_2^0 \rightarrow W^\pm \tilde{\chi}_1^\mp$
$\tilde{\chi}_2^0 \rightarrow \tilde{\chi}_1^- \nu_e e^+$	$2.48521683 \times 10^{-4}$	
$\tilde{\chi}_2^0 \rightarrow \tilde{\chi}_1^- \nu_\nu \mu^+$	$2.48521683 \times 10^{-4}$	
$\tilde{\chi}_2^0 \rightarrow \tilde{\chi}_1^+ d \bar{u}$	$7.45565048 \times 10^{-4}$	
$\tilde{\chi}_2^0 \rightarrow \tilde{\chi}_1^+ e^- \bar{\nu}_e$	$2.48521683 \times 10^{-4}$	
$\tilde{\chi}_2^0 \rightarrow \tilde{\chi}_1^+ \mu^- \bar{\nu}_\mu$	$2.48521683 \times 10^{-4}$	
$\tilde{\chi}_2^0 \rightarrow \tilde{\chi}_1^- c \bar{s}$	$7.45565048 \times 10^{-4}$	
$\tilde{\chi}_2^0 \rightarrow \tilde{\chi}_1^- \nu_\tau \tau^+$	$2.48521683 \times 10^{-4}$	
$\tilde{\chi}_2^0 \rightarrow \tilde{\chi}_1^+ s \bar{c}$	$7.45565048 \times 10^{-4}$	
$\tilde{\chi}_2^0 \rightarrow \tilde{\chi}_1^+ \tau^- \bar{\nu}_\tau$	$2.48521683 \times 10^{-4}$	
$\tilde{\chi}_2^0 \rightarrow \tilde{\chi}_1^0 u \bar{u}$	$1.25538409 \times 10^{-1}$	$\tilde{\chi}_2^0 \rightarrow q \bar{q} \tilde{\chi}_1^0$
$\tilde{\chi}_2^0 \rightarrow \tilde{\chi}_1^0 d \bar{d}$	$1.61880091 \times 10^{-1}$	
$\tilde{\chi}_2^0 \rightarrow \tilde{\chi}_1^0 s \bar{s}$	$1.61880091 \times 10^{-1}$	
$\tilde{\chi}_2^0 \rightarrow \tilde{\chi}_1^0 c \bar{c}$	$1.25538409 \times 10^{-1}$	
$\tilde{\chi}_2^0 \rightarrow \tilde{\chi}_1^0 b \bar{b}$	$9.05863643 \times 10^{-2}$	
$\tilde{\chi}_2^0 \rightarrow \tilde{\chi}_1^0 e^- e^+$	$3.67224030 \times 10^{-2}$	$\tilde{\chi}_2^0 \rightarrow \ell^+ \ell^- \tilde{\chi}_1^0$
$\tilde{\chi}_2^0 \rightarrow \tilde{\chi}_1^0 \mu^- \mu^+$	$3.67224030 \times 10^{-2}$	
$\tilde{\chi}_2^0 \rightarrow \tilde{\chi}_1^0 \tau^- \tau^+$	$3.35381366 \times 10^{-2}$	
$\tilde{\chi}_2^0 \rightarrow \tilde{\chi}_1^0 \nu_e \bar{\nu}_e$	$7.30678439 \times 10^{-2}$	$\tilde{\chi}_2^0 \rightarrow \nu \bar{\nu} \tilde{\chi}_1^0$
$\tilde{\chi}_2^0 \rightarrow \tilde{\chi}_1^0 \nu_\mu \bar{\nu}_\mu$	$7.30678439 \times 10^{-2}$	
$\tilde{\chi}_2^0 \rightarrow \tilde{\chi}_1^0 \nu_\tau \bar{\nu}_\tau$	$7.30678812 \times 10^{-2}$	

**Table 5.4:** The possible  $\tilde{\chi}_2^0$  decays in NUHM2 with  $m_{1/2} = 600$  GeV. The  $\tilde{\chi}_2^0 \rightarrow \gamma \tilde{\chi}_1^0$  has the lowest branching ratio hence it is not considered in our study. The rest of the decays are categorized into 4 types as shown in the third column.

Decay type	$\mathcal{BR}$	Filter efficiency			
		$pp \rightarrow \tilde{\chi}_2^0 \tilde{\chi}_1^+$	$pp \rightarrow \tilde{\chi}_2^0 \tilde{\chi}_1^-$	$N_{\text{event}}$	$N_{\text{event}}/N_{\text{total}}$
		$\tilde{\chi}_1^+ \rightarrow f \bar{f} \tilde{\chi}_1^0$	$\tilde{\chi}_1^- \rightarrow f \bar{f} \tilde{\chi}_1^0$		
$\tilde{\chi}_2^0 \rightarrow W^\pm \tilde{\chi}_1^\mp$	0.004473	0.117129	0.123213	1.032	0.377%
$\tilde{\chi}_2^0 \rightarrow q \bar{q} \tilde{\chi}_1^0$	0.665423	0.029174	0.028922	0.386	0.141%
$\tilde{\chi}_2^0 \rightarrow \ell^+ \ell^- \tilde{\chi}_1^0$	0.106983	0.605510	0.619579	272.463	99.482%
$\tilde{\chi}_2^0 \rightarrow \nu \bar{\nu} \tilde{\chi}_1^0$	0.219204	0.009555	0.010037	0	0.0%
All $\tilde{\chi}_2^0$ decays	1	-	-	273.881	100%

**Table 5.5:** The 2 leptons filter efficiency for 4 kinds of  $\tilde{\chi}_2^0$  decay, the number of events for each decay in  $0 < m_{\ell\ell} < 50$  GeV, and the contributions to the whole  $\tilde{\chi}_2^0$  decay. The transverse momentum of 2 leptons are required to be greater than 2 GeV and no  $E_{\text{T}}^{\text{miss}}$  requirement is applied in the filter.

## Chapter 6

### Event reconstruction and selection



## Chapter 7

### Background estimation

# Chapter 8

## Results

## Chapter 9

## Conclusion

# Appendix

# Appendix A

## Simulated samples

The Monte Carlo (MC) samples are used to model the SUSY signals and to estimate the SM background. The MC samples are processed using a ATLAS detector full simulation (FullSim) or a fast simulation (AFII<sup>1</sup>) based on GEANT4 [82] simulation package. The FullSim simulates the detailed properties of the ATLAS detector while the AFII uses a parameterized calorimeter response and simulates ID and MS [91] based on GEANT4. The simulated MC events are reweighted to the observed pile-up conditions in the data.

### A.1 Samples used for strong interaction

Table A.1 shows the event generator, parton shower, cross-section normalization, PDF set [86], and the set of tuned parameters for modelling for all samples. Except those produced by the SHERPA, the EVTGEN v1.2.0 package [88] is used to model the properties of bottom and charm hadron decays for all MC samples.

### A.2 Samples used for weak interaction

---

<sup>1</sup>AFII stands for ATLAS Fast II.

Signal/Background	Physics process	Event generator	Parton shower	Cross-section normalization	PDF set	Set of tuned parameters
Signal	RPC	MG5_AMC@NLO 2.2.3	PYTHIA 8.186	NLO+NLL	NNPDF2.3LO	A14
	RPV (except Figure ??)	MG5_AMC@NLO 2.2.3	PYTHIA 8.210	or	NNPDF2.3LO	A14
	RPV (Figure ??)	Herwig++ 2.7.1	Herwig++ 2.7.1	NLO-Prospino2	CTEQ6L1	UEEE5
$t\bar{t} + X$ background	$t\bar{t}W, t\bar{t}Z/\gamma^*$	MG5_AMC@NLO 2.2.2	PYTHIA 8.186	NLO	NNPDF2.3LO	A14
	$t\bar{t}H$	MG5_AMC@NLO 2.3.2	PYTHIA 8.186	NLO	NNPDF2.3LO	A14
	$4t$	MG5_AMC@NLO 2.2.2	PYTHIA 8.186	NLO	NNPDF2.3LO	A14
Diboson background	$ZZ, WZ$	SHERPA 2.2.1	SHERPA 2.2.1	NLO	NNPDF2.3LO	SHERPA default
	Other (inc. $W^\pm W^\pm$ )	SHERPA 2.1.1	SHERPA 2.1.1	NLO	CT10	SHERPA default
Rare background	$t\bar{t}WW, t\bar{t}WZ$	MG5_AMC@NLO 2.2.2	PYTHIA 8.186	NLO	NNPDF2.3LO	A14
	$tZ, tWZ, t\bar{t}\bar{t}$	MG5_AMC@NLO 2.2.2	PYTHIA 8.186	LO	NNPDF2.3LO	A14
	$WH, ZH$	MG5_AMC@NLO 2.2.2	PYTHIA 8.186	NLO	NNPDF2.3LO	A14
	Triboson	SHERPA 2.1.1	SHERPA 2.1.1	NLO	CT10	SHERPA default

**Table A.1:** The simulated signal and background MC samples. The event generator, parton shower, cross-section normalization, PDF set, and the set of tuned parameters for each samples are shown. The  $t\bar{t}WW, t\bar{t}WZ, tZ, tWZ, t\bar{t}\bar{t}, WH, ZH$  and triboson background samples are labeled in the "rare" because they contribute a very small amount to the signal region.

# Appendix B

## Cross-sections of NUHM2

The cross-sections, branching fraction, and filter efficiency for the NUHM2 signal samples are shown in Table [B.1](#), [B.2](#), [B.3](#), [B.4](#), [B.5](#), [B.6](#) and [B.7](#). The various final states are listed in Table [B.8](#)

DSID	Final state	Cross-section [ $pb$ ]	K-factor/BF	Filter efficiency	Relative uncertainty
370617	111	0.0116116904	1.00000000	1.00000000	0.07950234
370617	112	0.0009775530	1.00000000	1.00000000	0.08535312
370617	113	0.5163867234	1.00000000	1.00000000	0.07315089
370617	114	0.0000593483	1.00000000	1.00000000	0.08483826
370617	115	1.1555478731	1.00000000	1.00000000	0.06803190
370617	116	0.0056717958	1.00000000	1.00000000	0.05803524
370617	117	0.7027932124	1.00000000	1.00000000	0.08979719
370617	118	0.0030806972	1.00000000	1.00000000	0.07709474
370617	122	0.0000260248	1.00000000	1.00000000	0.13101757
370617	123	0.1709342503	1.00000000	1.00000000	0.06993300
370617	124	0.0002175469	1.00000000	1.00000000	0.08148442
370617	125	0.4768609298	1.00000000	1.00000000	0.06541649
370617	126	0.0228714654	1.00000000	1.00000000	0.05697991
370617	127	0.2784795051	1.00000000	1.00000000	0.08434059
370617	128	0.0120807622	1.00000000	1.00000000	0.07942795
370617	133	0.0003583977	1.00000000	1.00000000	0.06910802
370617	134	0.0191236271	1.00000000	1.00000000	0.06575101
370617	135	0.6773400626	1.00000000	1.00000000	0.06477621
370617	136	0.0262277631	1.00000000	1.00000000	0.05716003
370617	137	0.3954923581	1.00000000	1.00000000	0.08483868
370617	138	0.0137758494	1.00000000	1.00000000	0.08211888
370617	144	0.0000568127	1.00000000	1.00000000	0.07453184
370617	145	0.0213534960	1.00000000	1.00000000	0.05398319
370617	146	0.2119219378	1.00000000	1.00000000	0.05665419
370617	147	0.0113003976	1.00000000	1.00000000	0.07780129
370617	148	0.1028839844	1.00000000	1.00000000	0.07544194
370617	157	1.1640104660	1.00000000	1.00000000	0.07733674
370617	158	0.0187939524	1.00000000	1.00000000	0.06417211
370617	167	0.0188413722	1.00000000	1.00000000	0.06767782
370617	168	0.1655520687	1.00000000	1.00000000	0.06249944
394301	157	1.1640104660	0.1110699593	1.4334E-01	0.07733674
394302	127	0.2784795051	0.0365485123	2.5440E-01	0.08434059
394303	125	0.4768609298	0.0365485123	2.5135E-01	0.06541649
394304	112	0.0009775530	0.0365485123	3.0251E-01	0.08535312

**Table B.1:** The cross-sections, branching fraction, and filter efficiency for the NUHM2 signal samples  $m_{1/2} = 300$  GeV.



DSID	Final state	Cross-section [ $pb$ ]	K-factor/BF	Filter efficiency	Relative uncertainty
370618	111	0.0076283799	1.00000000	1.00000000	0.07739107
370618	112	0.5835187445	1.00000000	1.00000000	0.07193879
370618	113	0.0000894312	1.00000000	1.00000000	0.09912250
370618	114	0.0001023491	1.00000000	1.00000000	0.07825966
370618	115	1.0850849571	1.00000000	1.00000000	0.07591545
370618	116	0.0049251988	1.00000000	1.00000000	0.05689268
370618	117	0.6538672654	1.00000000	1.00000000	0.08886870
370618	118	0.0025928251	1.00000000	1.00000000	0.07604635
370618	122	0.0003076705	1.00000000	1.00000000	0.06756051
370618	123	0.1082826561	1.00000000	1.00000000	0.06926016
370618	124	0.0094622361	1.00000000	1.00000000	0.06300188
370618	125	0.6833463531	1.00000000	1.00000000	0.06443308
370618	126	0.0129259483	1.00000000	1.00000000	0.05402434
370618	127	0.3983657446	1.00000000	1.00000000	0.08599203
370618	128	0.0066391822	1.00000000	1.00000000	0.07534667
370618	133	0.0000649975	1.00000000	1.00000000	0.10705877
370618	134	0.0001247362	1.00000000	1.00000000	0.07583934
370618	135	0.2353276570	1.00000000	1.00000000	0.06552596
370618	136	0.0091529911	1.00000000	1.00000000	0.05672728
370618	137	0.1357101599	1.00000000	1.00000000	0.08410482
370618	138	0.0046580255	1.00000000	1.00000000	0.07466805
370618	144	0.0000282761	1.00000000	1.00000000	0.07380597
370618	145	0.0104731869	1.00000000	1.00000000	0.05738262
370618	146	0.1421425400	1.00000000	1.00000000	0.06087756
370618	147	0.0054325991	1.00000000	1.00000000	0.07452907
370618	148	0.0669626098	1.00000000	1.00000000	0.07470349
370618	157	0.9548695995	1.00000000	1.00000000	0.07280905
370618	158	0.0093028684	1.00000000	1.00000000	0.06338077
370618	167	0.0092973351	1.00000000	1.00000000	0.06299140
370618	168	0.1082938946	1.00000000	1.00000000	0.05684157
394305	157	0.9548695995	0.111060393	1.2990E-01	0.07280905
394306	127	0.3983657446	0.101384714	2.5255E-01	0.08599203
394307	125	0.6833463531	0.101384714	2.5574E-01	0.06443308
394308	112	0.5835187445	0.101384714	2.2766E-01	0.07193879

**Table B.2:** The cross-sections, branching fraction, and filter efficiency for the NUHM2 signal samples  $m_{1/2} = 350$  GeV.

DSID	Final state	Cross-section [ $pb$ ]	K-factor/BF	Filter efficiency	Relative uncertainty
370619	111	0.0050511346	1.00000000	1.00000000	0.07579917
370619	112	0.6255603991	1.00000000	1.00000000	0.07158509
370619	113	0.0000109243	1.00000000	1.00000000	0.09579487
370619	114	0.0001052946	1.00000000	1.00000000	0.07766307
370619	115	1.0342689914	1.00000000	1.00000000	0.06820123
370619	116	0.0035382215	1.00000000	1.00000000	0.05558890
370619	117	0.6163842668	1.00000000	1.00000000	0.08756721
370619	118	0.0018044868	1.00000000	1.00000000	0.07509790
370619	122	0.0002664650	1.00000000	1.00000000	0.07041738
370619	123	0.0628066056	1.00000000	1.00000000	0.06735393
370619	124	0.0048696810	1.00000000	1.00000000	0.06286865
370619	125	0.6845201512	1.00000000	1.00000000	0.06476776
370619	126	0.0067063042	1.00000000	1.00000000	0.05627793
370619	127	0.3976839861	1.00000000	1.00000000	0.08518583
370619	128	0.0033679821	1.00000000	1.00000000	0.07318125
370619	133	0.0000557211	1.00000000	1.00000000	0.10394707
370619	134	0.0000636446	1.00000000	1.00000000	0.07539568
370619	135	0.1183185424	1.00000000	1.00000000	0.05812791
370619	136	0.0036848994	1.00000000	1.00000000	0.05773533
370619	137	0.0670198462	1.00000000	1.00000000	0.08128406
370619	138	0.0018161476	1.00000000	1.00000000	0.07634830
370619	144	0.0000158930	1.00000000	1.00000000	0.07992644
370619	145	0.0054376416	1.00000000	1.00000000	0.05587952
370619	146	0.0976478188	1.00000000	1.00000000	0.06106615
370619	147	0.0027346724	1.00000000	1.00000000	0.07262348
370619	148	0.0442265190	1.00000000	1.00000000	0.07409153
370619	157	0.8415837349	1.00000000	1.00000000	0.07397928
370619	158	0.0047908009	1.00000000	1.00000000	0.06312184
370619	167	0.0047973169	1.00000000	1.00000000	0.06465433
370619	168	0.0724744359	1.00000000	1.00000000	0.06197995
394309	157	0.8415837349	0.111047482	1.2199E-01	0.07397928
394310	127	0.3976839861	0.102934938	2.2044E-01	0.08518583
394311	125	0.6845201512	0.102934938	2.2387E-01	0.06476776
394312	112	0.6255603991	0.102934938	2.0415E-01	0.07158509

**Table B.3:** The cross-sections, branching fraction, and filter efficiency for the NUHM2 signal samples  $m_{1/2} = 400$  GeV.

DSID	Final state	Cross-section [ $pb$ ]	K-factor/BF	Filter efficiency	Relative uncertainty
370620	111	0.0023867653	1.00000000	1.00000000	0.07209579
370620	112	0.6603094819	1.00000000	1.00000000	0.07005129
370620	113	0.0001325585	1.00000000	1.00000000	0.07482547
370620	114	0.0000688236	1.00000000	1.00000000	0.07197169
370620	115	0.9426500411	1.00000000	1.00000000	0.06460091
370620	116	0.0015013209	1.00000000	1.00000000	0.06183960
370620	117	0.5588686815	1.00000000	1.00000000	0.08560539
370620	118	0.0007279662	1.00000000	1.00000000	0.07490627
370620	122	0.0002061240	1.00000000	1.00000000	0.07176449
370620	123	0.0211437195	1.00000000	1.00000000	0.06388222
370620	124	0.0014907193	1.00000000	1.00000000	0.06151866
370620	125	0.6819165298	1.00000000	1.00000000	0.06356555
370620	126	0.0021061945	1.00000000	1.00000000	0.05664429
370620	127	0.3955900373	1.00000000	1.00000000	0.08416802
370620	128	0.0010081829	1.00000000	1.00000000	0.07123419
370620	133	0.0000195970	1.00000000	1.00000000	0.10671913
370620	134	0.0000176193	1.00000000	1.00000000	0.07871367
370620	135	0.0340389859	1.00000000	1.00000000	0.05924527
370620	136	0.0006926196	1.00000000	1.00000000	0.05800427
370620	137	0.0187411871	1.00000000	1.00000000	0.08099696
370620	138	0.0003229659	1.00000000	1.00000000	0.07606581
370620	144	0.0000098797	1.00000000	1.00000000	0.07455477
370620	145	0.0016797877	1.00000000	1.00000000	0.05654557
370620	146	0.0453186981	1.00000000	1.00000000	0.06092776
370620	147	0.0008077861	1.00000000	1.00000000	0.07385221
370620	148	0.0192295608	1.00000000	1.00000000	0.07792430
370620	157	0.7280789222	1.00000000	1.00000000	0.07328355
370620	158	0.0014642018	1.00000000	1.00000000	0.06676658
370620	167	0.0014587803	1.00000000	1.00000000	0.06499176
370620	168	0.0324683300	1.00000000	1.00000000	0.06503155
394313	157	0.7280789222	0.111019377	1.0812E-01	0.07328355
394314	127	0.3955900373	0.105384522	1.8923E-01	0.08416802
394315	125	0.6819165298	0.105384522	1.8805E-01	0.06356555
394316	112	0.6603094819	0.105384522	1.7600E-01	0.07005129

**Table B.4:** The cross-sections, branching fraction, and filter efficiency for the NUHM2 signal samples  $m_{1/2} = 500$  GeV.

DSID	Final state	Cross-section [ $pb$ ]	K-factor/BF	Filter efficiency	Relative uncertainty
370621	111	0.0012897690	1.00000000	1.00000000	0.07308455
370621	112	0.6656504736	1.00000000	1.00000000	0.07047924
370621	113	0.0001361496	1.00000000	1.00000000	0.07047382
370621	114	0.0000378018	1.00000000	1.00000000	0.07036880
370621	115	0.8824882181	1.00000000	1.00000000	0.06538492
370621	116	0.0006132703	1.00000000	1.00000000	0.05826096
370621	117	0.5187808653	1.00000000	1.00000000	0.08546879
370621	118	0.0002849360	1.00000000	1.00000000	0.07563404
370621	122	0.0001627043	1.00000000	1.00000000	0.06980768
370621	123	0.0078958339	1.00000000	1.00000000	0.06365983
370621	124	0.0005370949	1.00000000	1.00000000	0.06338450
370621	125	0.6791453722	1.00000000	1.00000000	0.06375124
370621	126	0.0007771667	1.00000000	1.00000000	0.05779085
370621	127	0.3930396433	1.00000000	1.00000000	0.08337329
370621	128	0.0003583832	1.00000000	1.00000000	0.07532675
370621	133	0.0000068529	1.00000000	1.00000000	0.09776310
370621	134	0.0000060514	1.00000000	1.00000000	0.07178228
370621	135	0.0118585454	1.00000000	1.00000000	0.06459092
370621	136	0.0001672449	1.00000000	1.00000000	0.05977911
370621	137	0.0063210120	1.00000000	1.00000000	0.07773831
370621	138	0.0000738669	1.00000000	1.00000000	0.07600501
370621	144	0.0000050854	1.00000000	1.00000000	0.10988000
370621	145	0.0006099769	1.00000000	1.00000000	0.05679637
370621	146	0.0230198632	1.00000000	1.00000000	0.06402567
370621	147	0.0002805066	1.00000000	1.00000000	0.07646096
370621	148	0.0091676826	1.00000000	1.00000000	0.07848717
370621	157	0.6745140438	1.00000000	1.00000000	0.07398616
370621	158	0.0005268754	1.00000000	1.00000000	0.06482055
370621	167	0.0005263009	1.00000000	1.00000000	0.06458416
370621	168	0.0159949974	1.00000000	1.00000000	0.06360196
394317	157	0.6745140438	0.110994804	9.9998E-02	0.07398616
394318	127	0.3930396433	0.107603552	1.6870E-01	0.08337329
394319	125	0.6791453722	0.107603552	1.6924E-01	0.06375124
394320	112	0.6656504736	0.107603552	1.5353E-01	0.07047924

**Table B.5:** The cross-sections, branching fraction, and filter efficiency for the NUHM2 signal samples  $m_{1/2} = 600$  GeV.

DSID	Final state	Cross-section [ $pb$ ]	K-factor/BF	Filter efficiency	Relative uncertainty
370622	111	0.0007869897	1.00000000	1.00000000	0.07181679
370622	112	0.6643270342	1.00000000	1.00000000	0.07021531
370622	113	0.0000996207	1.00000000	1.00000000	0.06721434
370622	114	0.0000204490	1.00000000	1.00000000	0.07299332
370622	115	0.8407296201	1.00000000	1.00000000	0.06552209
370622	116	0.0002658841	1.00000000	1.00000000	0.06040295
370622	117	0.4923724748	1.00000000	1.00000000	0.08491961
370622	118	0.0001190742	1.00000000	1.00000000	0.08405305
370622	122	0.0001324452	1.00000000	1.00000000	0.07307817
370622	123	0.0033217150	1.00000000	1.00000000	0.06361965
370622	124	0.0002184464	1.00000000	1.00000000	0.06456221
370622	125	0.6766070496	1.00000000	1.00000000	0.06427279
370622	126	0.0003241413	1.00000000	1.00000000	0.05818056
370622	127	0.3913281838	1.00000000	1.00000000	0.08575382
370622	128	0.0001431279	1.00000000	1.00000000	0.07221632
370622	133	0.0000034045	1.00000000	1.00000000	0.08794933
370622	134	0.0000026928	1.00000000	1.00000000	0.07609993
370622	135	0.0048337927	1.00000000	1.00000000	0.05703733
370622	136	0.0000502367	1.00000000	1.00000000	0.06355969
370622	137	0.0025078220	1.00000000	1.00000000	0.07562175
370622	138	0.0000209783	1.00000000	1.00000000	0.07847390
370622	144	0.0000052666	1.00000000	1.00000000	0.07856700
370622	145	0.0002494848	1.00000000	1.00000000	0.06059516
370622	146	0.0118318988	1.00000000	1.00000000	0.07046938
370622	147	0.0001094560	1.00000000	1.00000000	0.07805891
370622	148	0.0044453542	1.00000000	1.00000000	0.08306247
370622	157	0.6438838471	1.00000000	1.00000000	0.07295880
370622	158	0.0002140543	1.00000000	1.00000000	0.06775447
370622	167	0.0002138494	1.00000000	1.00000000	0.06731630
370622	168	0.0079546496	1.00000000	1.00000000	0.06899943
394321	157	0.6438838471	0.110976399	9.3533E-02	0.07295880
394322	127	0.3913281838	0.109700775	1.5801E-01	0.08575382
394323	125	0.6766070496	0.109700775	1.5871E-01	0.06427279
394324	112	0.6643270342	0.109700775	1.3786E-01	0.07021531

**Table B.6:** The cross-sections, branching fraction, and filter efficiency for the NUHM2 signal samples  $m_{1/2} = 700$  GeV.

DSID	Final state	Cross-section [ $pb$ ]	K-factor/BF	Filter efficiency	Relative uncertainty
370623	111	0.0005212386	1.00000000	1.00000000	0.07063351
370623	112	0.6598118363	1.00000000	1.00000000	0.06943069
370623	113	0.0000669873	1.00000000	1.00000000	0.06712724
370623	114	0.0000113016	1.00000000	1.00000000	0.07064093
370623	115	0.8098002978	1.00000000	1.00000000	0.06493814
370623	116	0.0001234140	1.00000000	1.00000000	0.06889051
370623	117	0.4737135796	1.00000000	1.00000000	0.08608973
370623	118	0.0000526249	1.00000000	1.00000000	0.07771427
370623	122	0.0001087675	1.00000000	1.00000000	0.07088280
370623	123	0.0015416626	1.00000000	1.00000000	0.06537577
370623	124	0.0000974637	1.00000000	1.00000000	0.06530325
370623	125	0.6748686972	1.00000000	1.00000000	0.06282954
370623	126	0.0001487367	1.00000000	1.00000000	0.06359830
370623	127	0.3906074836	1.00000000	1.00000000	0.08243869
370623	128	0.0000632347	1.00000000	1.00000000	0.07613879
370623	133	0.0000021556	1.00000000	1.00000000	0.08808178
370623	134	0.0000013753	1.00000000	1.00000000	0.08184458
370623	135	0.0022215540	1.00000000	1.00000000	0.05781810
370623	136	0.0000179127	1.00000000	1.00000000	0.06707128
370623	137	0.0011306653	1.00000000	1.00000000	0.07974272
370623	138	0.0000071002	1.00000000	1.00000000	0.07996818
370623	144	0.0000033200	1.00000000	1.00000000	0.08521909
370623	145	0.0001114849	1.00000000	1.00000000	0.06626951
370623	146	0.0064128038	1.00000000	1.00000000	0.07356448
370623	147	0.0000474513	1.00000000	1.00000000	0.07695978
370623	148	0.0023333882	1.00000000	1.00000000	0.08950999
370623	157	0.6240319555	1.00000000	1.00000000	0.07242344
370623	158	0.0000960852	1.00000000	1.00000000	0.06651898
370623	167	0.0000961123	1.00000000	1.00000000	0.06811969
370623	168	0.0042577101	1.00000000	1.00000000	0.07239458
394325	157	0.6240319555	0.1109638923	8.7153E-02	0.07242344
394326	127	0.3906074836	0.1116429166	1.3865E-01	0.08243869
394327	125	0.6748686972	0.1116429166	1.4629E-01	0.06282954
394328	112	0.6598118363	0.1116429166	1.2823E-01	0.06943069

**Table B.7:** The cross-sections, branching fraction, and filter efficiency for the NUHM2 signal samples  $m_{1/2} = 800$  GeV.

ID	Particles	ID	Particles	ID	Particles	ID	Particles	ID	Particles	ID	Particles
111	$\chi_1^0 \chi_1^0$	-	-	-	-	-	-	-	-	-	-
112	$\chi_1^0 \chi_2^0$	122	$\chi_2^0 \chi_2^0$	-	-	-	-	-	-	-	-
113	$\chi_1^0 \chi_3^0$	123	$\chi_2^0 \chi_3^0$	133	$\chi_3^0 \chi_3^0$	-	-	-	-	-	-
114	$\chi_1^0 \chi_4^0$	124	$\chi_2^0 \chi_4^0$	134	$\chi_3^0 \chi_4^0$	144	$\chi_4^0 \chi_4^0$	-	-	-	-
115	$\chi_1^0 \chi_1^+$	125	$\chi_2^0 \chi_1^+$	135	$\chi_3^0 \chi_1^+$	145	$\chi_4^0 \chi_1^+$	-	-	-	-
116	$\chi_1^0 \chi_2^+$	126	$\chi_2^0 \chi_2^+$	136	$\chi_3^0 \chi_2^+$	146	$\chi_4^0 \chi_2^+$	-	-	-	-
117	$\chi_1^0 \chi_1^-$	127	$\chi_2^0 \chi_1^-$	137	$\chi_3^0 \chi_1^-$	147	$\chi_4^0 \chi_1^-$	157	$\chi_1^+ \chi_1^-$	167	$\chi_2^+ \chi_1^-$
118	$\chi_1^0 \chi_2^-$	128	$\chi_2^0 \chi_2^-$	138	$\chi_3^0 \chi_2^-$	148	$\chi_4^0 \chi_2^-$	158	$\chi_1^+ \chi_2^-$	168	$\chi_2^+ \chi_2^-$

**Table B.8:** The list of various final states.

# Appendix C

## Electron reconstruction, identification, and isolation

The electron reconstruction, identification, and isolation play a crucial role for many ATLAS analysis. The electrons<sup>1</sup> leave tracks in the ID and energy deposits in the ECAL. The reconstruction algorithm combines the signals in the calorimeter and the tracks in the ID to defined the electron candidates. The reconstructed candidates are identified as electrons based on a likelihood discrimination which distinguishes the electron candidates from the hadrons, non-prompt electrons originating from photon conversions, and heavy flavour hadron decays. Additionally, the electron candidates are required to be isolated to further distinguish the signal and the background objects. The electron efficiency measurements are performed based on the tag-and-probe method using the  $Z \rightarrow ee$  and  $J/\psi \rightarrow ee$  samples.

### C.1 Electron reconstruction

The electrons are reconstructed in the central region of the ATLAS detector ( $|\eta| < 2.47$ ).

---

<sup>1</sup>The electrons and positron are referred to as electrons.



## **C.2   Electron identification**

## **C.3   Electron isolation**

## Appendix D

### Real lepton efficiency

# References

- [1] Georges Aad et al. Observation of a new particle in the search for the Standard Model Higgs boson with the ATLAS detector at the LHC. *Phys. Lett.*, B716:1–29, 2012. ([document](#)), [1](#), [2.1.5](#), [2.2](#)
- [2] Serguei Chatrchyan et al. Observation of a new boson at a mass of 125 GeV with the CMS experiment at the LHC. *Phys. Lett.*, B716:30–61, 2012. ([document](#)), [1](#), [2.1.5](#), [2.2](#)
- [3] Steven Weinberg. Implications of Dynamical Symmetry Breaking. *Phys. Rev.*, D13:974–996, 1976. [Addendum: *Phys. Rev.*D19,1277(1979)]. [1](#)
- [4] Eldad Gildener. Gauge Symmetry Hierarchies. *Phys. Rev.*, D14:1667, 1976. [1](#)
- [5] Leonard Susskind. Dynamics of Spontaneous Symmetry Breaking in the Weinberg-Salam Theory. *Phys. Rev.*, D20:2619–2625, 1979. [1](#)
- [6] J. Wess and B. Zumino. A Lagrangian Model Invariant Under Supergauge Transformations. *Phys. Lett.*, 49B:52, 1974. [1](#)
- [7] J Wess and B Zumino. Supergauge transformations in four dimensions. *Nucl. Phys. B*, 70(CERN-TH-1753. 1):39–50, 1974. [1](#)
- [8] Yu. A. Golfand and E. P. Likhtman. Extension of the Algebra of Poincare Group Generators and Violation of p Invariance. *JETP Lett.*, 13:323–326, 1971. [Pisma Zh. Eksp. Teor. Fiz.13,452(1971)]. [1](#)
- [9] Stephen P. Martin. A Supersymmetry primer. 1997. [Adv. Ser. Direct. High Energy Phys.18,1(1998)]. ([document](#)), [1](#), [2.2.1](#), [3](#), [3.1](#)
- [10] Pierre Fayet. Supersymmetry and Weak, Electromagnetic and Strong Interactions. *Phys. Lett.*, 64B:159, 1976. [1](#)
- [11] Pierre Fayet. Spontaneously Broken Supersymmetric Theories of Weak, Electromagnetic and Strong Interactions. *Phys. Lett.*, 69B:489, 1977. [1](#)
- [12] Glennys R. Farrar and Pierre Fayet. Phenomenology of the Production, Decay, and Detection of New Hadronic States Associated with Supersymmetry. *Phys. Lett.*, 76B:575–579, 1978. [1](#)
- [13] Morad Aaboud et al. Dark matter interpretations of ATLAS searches for the electroweak production of supersymmetric particles in  $\sqrt{s} = 8$  TeV proton-proton collisions. *JHEP*, 09:175, 2016. ([document](#)), [1](#), [1.1](#), [1](#)

- [14] Riccardo Barbieri and G. F. Giudice. Upper Bounds on Supersymmetric Particle Masses. *Nucl. Phys.*, B306:63–76, 1988. [1](#)
- [15] B. de Carlos and J. A. Casas. One loop analysis of the electroweak breaking in supersymmetric models and the fine tuning problem. *Phys. Lett.*, B309:320–328, 1993. [1](#)
- [16] Lyndon Evans and Philip Bryant. LHC Machine. *JINST*, 3:S08001, 2008. [1](#)
- [17] Georges Aad et al. Search for direct production of charginos, neutralinos and sleptons in final states with two leptons and missing transverse momentum in  $pp$  collisions at  $\sqrt{s} = 8$  TeV with the ATLAS detector. *JHEP*, 05:071, 2014. [1](#)
- [18] Georges Aad et al. Search for direct production of charginos and neutralinos in events with three leptons and missing transverse momentum in  $\sqrt{s} = 8$ TeV  $pp$  collisions with the ATLAS detector. *JHEP*, 04:169, 2014. [1](#)
- [19] Georges Aad et al. Search for the electroweak production of supersymmetric particles in  $\sqrt{s}=8$  TeV  $pp$  collisions with the ATLAS detector. *Phys. Rev.*, D93(5):052002, 2016. [1](#)
- [20] Vardan Khachatryan et al. Searches for electroweak production of charginos, neutralinos, and sleptons decaying to leptons and W, Z, and Higgs bosons in pp collisions at 8 TeV. *Eur. Phys. J.*, C74(9):3036, 2014. [1](#)
- [21] Vardan Khachatryan et al. Search for supersymmetry in events with soft leptons, low jet multiplicity, and missing transverse energy in protonproton collisions at  $\sqrt{s}=8$  TeV. *Phys. Lett.*, B759:9–35, 2016. [1](#)
- [22] Albert M Sirunyan et al. Search for electroweak production of charginos and neutralinos in multilepton final states in proton-proton collisions at  $\sqrt{s} = 13$  TeV. 2017. [1](#)
- [23] Abdus Salam and J.C. Ward. Weak and electromagnetic interactions. *Nuovo Cimento*, 11(4):568–577, Feb 1959. [2](#), [2.1.4](#), [3](#)
- [24] Sheldon L. Glashow. Partial-symmetries of weak interactions. *Nuclear Physics*, 22(4):579–588, Feb 1961. [2](#), [2.1.4](#), [3](#)
- [25] Steven Weinberg. A model of leptons. *Phys. Rev. Lett.*, 19(21):1264–1266, Nov 1967. [2](#), [2.1.4](#), [3](#)
- [26] M. Herrero. The standard model. *NATO Sci. Ser. C*, 534:1–59, 1999. [2](#), [3](#)
- [27] D. A. Greenwood W. N. Cottingham. *An Introduction to the Standard Model of Particle Physics*. Cambridge University Press, 2 edition, 2007. [2](#), [3](#)
- [28] Emmy Noether. Invariant variation problems. *Transport Theory and Statistical Physics*, 1(3):186–207, 1971. [2.1](#)
- [29] K.A. Olive et al (Particle Data Group). Review of particle physics. *Chin. Phys. C*, 38(9):090001, 2014. [\(document\)](#), [2.1](#), [2.1.1](#)

- [30] E. Fermi. Versuch einer theorie der  $\gamma$ -strahlen. i. *Zeitschrift für Physik*, 88(3-4):161–177, Mar 1934. [2.1.4](#)
- [31] Tadao Nakano and Kazuhiko Nishijima. Charge independence for  $\nu$ -particles. *Progress of Theoretical Physics*, 10(5):581–582, 1953. [2.1.4](#)
- [32] M. Gell-Mann. The interpretation of the new particles as displaced charge multiplets. *Nuovo Cim*, 4(2):848–866, Apr 1956. [2.1.4](#)
- [33] Makoto Kobayashi and Toshihide Maskawa.  $C_P$ -violation in the renormalizable theory of weak interaction. *Progress of Theoretical Physics*, 49(2):652–657, Feb 1973. [2.1.4](#)
- [34] Ziro Maki, Masami Nakagawa, and Shoichi Sakata. Remarks on the unified model of elementary particles. *Progress of Theoretical Physics*, 28(5):870–880, Nov 1962. [2.1.4](#)
- [35] Peter W. Higgs. Spontaneous symmetry breakdown without massless bosons. *Phys. Rev.*, 145(4):1156–1163, May 1964. [2.1.4](#)
- [36] Peter W. Higgs. Broken symmetries and the masses of gauge bosons. *Phys. Rev. Lett.*, 13(16):508–509, Oct 1964. [2.1.4](#)
- [37] Peter W. Higgs. Broken symmetries, massless particles and gauge fields. *Physics Letters*, 12(2):132–133, Sept 1964. [2.1.4](#)
- [38] F. Englert and R. Brout. Broken symmetry and the mass of gauge vector mesons. *Phys. Rev. Lett.*, 13(9):321–323, Aug 1964. [2.1.4](#)
- [39] G. S. Guralnik, C. R. Hagen, and T. W. B. Kibble. Global conservation laws and massless particles. *Phys. Rev. Lett.*, 13(20):585–587, Nov 1964. [2.1.4](#)
- [40] John Ellis. Higgs physics. *arXiv*, arXiv:1312.5672v1, 2015. ([document](#)), [2.1](#)
- [41] Piotr H. Chankowskia, John Ellisb, Keith A.Olivec, and Stefan Pokorskia. Cosmological fine tuning, supersymmetry and the gauge hierarchy problem. *Physics Letters B*, 452(1-2):28–38, Apr 1999. [2.2.1](#)
- [42] Maarten C. Brak. The hierarchy problem in the standard model and little higgs theories. Oct 2004. [2.2.1](#)
- [43] WMAP Collaboration. Nine-year wilkinson microwave anisotropy probe (wmap) observations: Final maps and results. *arXiv*, arXiv:1212.5225v3 [astro-ph.CO], 2012. [2.2.2](#)
- [44] P. A. R. Ade et al. Planck 2013 results. i. overview of products and scientific results. *Astron. Astrophys.*, 571, 2014. [2.2.2](#)
- [45] Gianfranco Bertone, Dan Hooper, and Joseph Silk. Particle dark matter: evidence, candidates and constraints. *Physics Reports*, 405(5-6):279–390, 2005. [2.2.2](#)
- [46] G. Ross. Grand unified theories: Frontiers in physics. *Physics Bulletin*, 37(10):429, 1986. [2.2.3](#)
- [47] Peter J. Mohr, Barry N. Taylor, and David B. Newell. Codata recommended values of the fundamental physical constants: 2010. *Rev. Mod. Phys.*, 84(4):1527–1605, Nov 2012. [2.2.3](#)

- [48] [\(document\)](#), [2.3](#)
- [49] J. Wess and B. Zumino. Supergauge transformations in four dimensions. *Nucl. Phys. B*, 70(1):39–50, Feb 1974. [3](#)
- [50] Joseph D. Lykken. Introduction to supersymmetry. *arXiv*, hep-th/9612114v1, Dec 1996. [3](#)
- [51] Manuel Drees. An introduction to supersymmetry. *arXiv*, hep-ph/9611409v1, Nov 1996. [3](#)
- [52] Adel Bilal. Introduction to supersymmetry. *arXiv*, hep-th/0101055v1, Jan 2001. [3](#)
- [53] Philip C. Argyres. An introduction to global supersymmetry. 2001. [3](#)
- [54] Michael E. Peskin. Supersymmetry in elementary particle physics. *arXiv*, 0801.1928v1, 2008. [3](#)
- [55] Ian Aitchison. *Supersymmetry in Particle Physics*. Cambridge University Press, Sept 2012. [3](#)
- [56] Y. Shadmi. Introduction to supersymmetry. *arXiv*, 1708.00772v1, Aug 2017. [3](#)
- [57] Howard Baer, Vernon Barger, Peisi Huang, Dan Mickelson, Azar Mustafayev, Warintorn Sreethawong, and Xerxes Tata. Radiatively-driven natural supersymmetry at the LHC. *JHEP*, 12:013, 2013. [Erratum: JHEP06,053(2015)]. [3.3](#), [5.2.2](#)
- [58] Howard Baer, Vernon Barger, Peisi Huang, Azar Mustafayev, and Xerxes Tata. Radiative natural SUSY with a 125 GeV Higgs boson. *Phys. Rev. Lett.*, 109:161802, 2012. [3.3](#)
- [59] Howard Baer. Radiative natural supersymmetry with mixed axion/higgsino cold dark matter. 2012. [AIP Conf. Proc.1534,39(2012)]. [3.3](#)
- [60] Howard Baer, Vernon Barger, Peisi Huang, Dan Mickelson, Azar Mustafayev, and Xerxes Tata. Radiative natural supersymmetry: Reconciling electroweak fine-tuning and the Higgs boson mass. *Phys. Rev.*, D87(11):115028, 2013. [3.3](#)
- [61] John R. Ellis, Keith A. Olive, and Yudi Santoso. The MSSM parameter space with nonuniversal Higgs masses. *Phys. Lett.*, B539:107–118, 2002. [3.4](#)
- [62] John R. Ellis, Toby Falk, Keith A. Olive, and Yudi Santoso. Exploration of the MSSM with nonuniversal Higgs masses. *Nucl. Phys.*, B652:259–347, 2003. [3.4](#)
- [63] Howard Baer, Azar Mustafayev, Stefano Profumo, Alexander Belyaev, and Xerxes Tata. Neutralino cold dark matter in a one parameter extension of the minimal supergravity model. *Phys. Rev.*, D71:095008, 2005. [3.4](#)
- [64] Howard Baer, Azar Mustafayev, Stefano Profumo, Alexander Belyaev, and Xerxes Tata. Direct, indirect and collider detection of neutralino dark matter in SUSY models with non-universal Higgs masses. *JHEP*, 07:065, 2005. [3.4](#)
- [65] Lyndon Evans and Philip Bryant. Lhc machine. *Journal of Instrumentation*, 3(08):S08001, 2008. [4](#), [4.1](#), [4.2](#)

- [66] The ATLAS Collaboration. The atlas experiment at the cern large hadron collider. *Journal of Instrumentation*, 3(08):S08003, 2008. ([document](#)), [4](#), [4.2](#), [4.2](#), [4.3](#), [4.4](#), [4.2.3](#), [4.1](#), [4.2.4](#), [4.6](#)
- [67] The CMS Collaboration. The cms experiment at the cern lhc. *Journal of Instrumentation*, 3(08):S08004, 2008. [4](#)
- [68] The ALICE Collaboration. The alice experiment at the cern lhc. *Journal of Instrumentation*, 3(08):S08002, 2008. [4](#)
- [69] The LHCb Collaboration. The lhcb detector at the lhc. *Journal of Instrumentation*, 3(08):S08005, 2008. [4](#)
- [70] The TOTEM Collaboration. The totem experiment at the cern large hadron collider. *Journal of Instrumentation*, 3(08):S08007, 2008. [4](#)
- [71] The LHCf Collaboration. The lhcf detector at the cern large hadron collider. *Journal of Instrumentation*, 3(08):S08006, 2008. [4](#)
- [72] James Pinfold, R Soluk, Y Yao, S Cecchini, G Giacomelli, M Giorgini, L Patrizii, G Sirri, D H Lacarrère, K Kinoshita, J Jakubek, M Platkevic, S Pospíšil, Z Vykydal, T Hott, A Houdayer, Claude Leroy, J Swain, D Felea, D Hasegan, G E Pavallas, and V” Popa. Technical design report of the moedal experiment. *CERN-LHCC-2009-006*, CERN-LHCC-2009-006(MoEDAL-TDR-001), Jun 2009. [4](#)
- [73] Fabienne Marcastel. Cern’s accelerator complex. la chaîne des accélérateurs du cern. *OPEN-PHO-CHART-2013-001*, Oct 2013. ([document](#)), [4.1](#)
- [74] L. Rossi. The lhc superconducting magnets. In *Proceedings of the 2003 Particle Accelerator Conference*, volume 1, pages 141–145 Vol.1, May 2003. [4.1](#)
- [75] The lhc sees its first circulating beam. [4.1](#)
- [76] Nikiforos Nikiforou. Performance of the atlas liquid argon calorimeter after three years of lhc operation and plans for a future upgrade. *arXiv*, arXiv:1306.6756v2, Jun 2013. ([document](#)), [4.5](#)
- [77] S Palestini. The muon spectrometer of the atlas experiment. Technical Report ATL-MUON-2004-001, CERN, Geneva, Feb 2003. Contribution to the proceedings : 8th Topical Seminar on Innovative Particle and Radiation Detectors, 21-24 Oct. 2002, Siena, Italy. [4.2.4](#)
- [78] ATLAS muon collaboration. Atlas muon detector commissioning. *arXiv*, arXiv:0910.2767v1, 2009. [4.2.4](#)
- [79] The ATLAS Collaboration. The atlas data acquisition and trigger: concept, design and status. *Nucl. Phys. B Proc. Suppl.*, 172:178–182, Oct 2007. [4.2.5](#)
- [80] The ATLAS Collaboration. The run-2 atlas trigger system. *J. Phys. Conf. Ser.*, 762(1):012003, Feb 2016. ([document](#)), [4.7](#)
- [81] Morad Aaboud et al. Luminosity determination in pp collisions at  $\sqrt{s} = 8$  TeV using the ATLAS detector at the LHC. *Eur. Phys. J.*, C76(12):653, 2016. [5.1](#)

- [82] S. Agostinelli et al. GEANT4: A Simulation toolkit. *Nucl. Instrum. Meth.*, A506:250–303, 2003. [5.2](#), [A](#)
- [83] ATLAS Collaboration. The simulation principle and performance of the ATLAS fast calorimeter simulation FastCaloSim. 2010. [5.2](#)
- [84] Torbjorn Sjostrand, Stephen Mrenna, and Peter Z. Skands. A Brief Introduction to PYTHIA 8.1. *Comput. Phys. Commun.*, 178:852–867, 2008. [5.2](#)
- [85] Summary of ATLAS Pythia 8 tunes. 2012. [5.2](#)
- [86] A. D. Martin, W. J. Stirling, R. S. Thorne, and G. Watt. Parton distributions for the LHC. *Eur. Phys. J.*, C63:189–285, 2009. [5.2](#), [A.1](#)
- [87] T. Gleisberg, Stefan. Hoeche, F. Krauss, M. Schonherr, S. Schumann, F. Siegert, and J. Winter. Event generation with SHERPA 1.1. *JHEP*, 02:007, 2009. [5.2.1](#)
- [88] D. J. Lange. The EvtGen particle decay simulation package. *Nucl. Instrum. Meth.*, A462:152–155, 2001. [5.2.1](#), [A.1](#)
- [89] Howard Baer, Frank E. Paige, Serban D. Protopopescu, and Xerxes Tata. ISAJET 7.48: A Monte Carlo event generator for p p, anti-p, p, and e+ e- reactions. 1999. [5.2.2](#)
- [90] W. Beenakker, M. Klasen, M. Kramer, T. Plehn, M. Spira, and P. M. Zerwas. The Production of charginos / neutralinos and sleptons at hadron colliders. *Phys. Rev. Lett.*, 83:3780–3783, 1999. [Erratum: *Phys. Rev. Lett.*100,029901(2008)]. [5.2.2](#)
- [91] Coll ATLAS, M Beckingham, M Duehrssen, E Schmidt, M Shapiro, M Venturi, J Virzi, I Vivarelli, M Werner, S Yamamoto, and T Yamanaka. The simulation principle and performance of the ATLAS fast calorimeter simulation FastCaloSim. Technical Report ATL-PHYS-PUB-2010-013, CERN, Geneva, Oct 2010. [A](#)